NASA Contractor Report 172368

NASA-CR-172368
19840021083

THREE-DIMENSIONAL UNSTEADY VISCOUS FLOW ANALYSIS OVER AIRFOIL SECTIONS

Bernard C. Weinberg, Stephen J. Shamroth

Scientific Research Associates, Inc.

Glastonbury, CT. 06033

Contract NAS1-17573

JUNE 1984

NASA
National Aeronautics and
Space Administration

Langley Research Center
Hampton, Virginia 23665

Three-dimensional unsteady viscous effects can significantly influence the performance of fixed wing and rotary wing aircraft. These effects are important in particular for the flow about a helicopter rotor in forward flight and the flow about a three-dimensional (swept and tapered) supercritical wing at transonic speeds. In both cases, the viscous boundary layer is predominantly thin and exhibits regions of reverse flow in the streamwise and/or spanwise direction. Clearly a computational procedure that can calculate such flow fields would be of great value in the design process as well as in understanding the flow phenomena.

A new computational procedure specifically designed to handle such problems has been developed which bridges the gap between the inviscid/boundary layer and Navier-Stokes approaches in that it is of sufficient generality to compute regions of reverse flow yet is efficient and user-oriented. Hence, the major objectives of the current effort were to adapt this technique to treat three-dimensional unsteady turbulent flows and validate the procedure by comparing the predictions to experimenal data.

These goals have been achieved by considering the experimental data of Karlsson, i.e. two-dimensional unsteady oscillating turbulent flow over a flat plate. Two-dimensional calculations were performed and the results agreed both qualitatively and quantitatively with the data. Thereafter, the analagous three-dimensional case was considered which was obtained by a coordinate rotation to yield the flow over a flate plate skewed at 45° to the freestream direction. The results of this computation also agreed well with both the two-dimensional results and Karlsson's data, hence validating the computational procedure in three dimensions. In addition, new inflow boundary conditions were developed and an explanation was proposed to resolve the discrepancy concerning other previously reported predictions of the skin friction phase lead angle as a function of reduced frequency.

The computational procedure which has been validated in the Phase I effort can have a significant impact in the design of both rotary and fixed wings by predicting the onset of separation and the flow properties through regions of reverse flow. In addition, with the inclusion of a displacment thickness interaction option, the procedure can be made more general and can aid in transonic flutter and buffet aerodynamic analyses where interaction is important. Furthermore, the calculation procedure can be extended to handle oscillating control surfaces in a three-dimensional flow.

ANALYSIS

Introduction

In recent years there has been increased attention given to three-dimensional unsteady aerodynamics. Such flows manifest themselves over fixed wing and rotary wing aircraft. Fixed wing aircraft are designed to be nominally steady with the unsteady effects being introduced through either control surface motions or induced external oscillations. These phenomena are observed in flow about wings throughout the Mach number regime; subsonic, transonic, and supersonic. The unsteady effects will influence loss levels as well as lift and moment coefficients. As the speed increases beyond subsonic into the transonic regime, additional effects such as flutter, buffeting and aileron buzz may arise. Since the new generation of energy efficient transports will be operating in the transonic range, the prediction of the onset of these phenomena under transonic conditions will play a significant role in the design process. Furthermore, the accurate prediction of the aerodynamic loading during the unsteady flow phase is crucial in prescribing the correct input for aeroelastic analyses. As a result of the three-dimensional nature of the transonic supercritical wings i.e. taper and sweep, the flow structure will be three-dimensional, while the oscillating recompression shock will cause regions of reverse flow to exist in the streamwise and/or spanwise directions.

In contrast to fixed winged aircraft, the flow about a rotary wing is designed to operate in an unsteady environment. The flow about a helicopter rotor in forward flight is periodic and exhibits substantial unsteady transonic effects. As a consequence of the vortex-wake interaction of the advancing blades, broad band frequencies are excited having large amplitude oscillations relative to the blade. This flow is also highly three-dimensional with regions of reverse flow existing in the streamwise and spanwise directions.

Concurrent with these developments has been an increased effort to better understand these phenomena by conducting three-dimensional unsteady wing experimental programs (cf. Ref. 1, 2) and applying inviscid computational procedures to these problems (e.g. Ref. 3, 4). The results of the numerical calculations in conjunction with the experimental data

indicate that the observed phenomena are strongly influenced by viscous effects near the body surface which are not accounted for by the inviscid predictions. These viscous effects are concentrated within a region that is predominately thin except for localized regions of reverse flow in the streamwise and/or spanwise directions. Hence, there is clearly a need to compute these viscous effects in an efficient and economical manner.

There are several possible approaches available for computing three-dimensional viscous flows, ranging from empirical models to sophisticated treatments based on the solution of the three-dimensional time-dependent Navier-Stokes equations. Due to the complex structure of the flow the empirical approach is too restrictive. At the other end of the spectrum is the three-dimensional time-dependent Navier-Stokes analysis. Even though such procedures have been developed at SRA and have been applied successfully to a variety of problems (Refs. 5, 6, 7), such a technique is not required for many of the viscous layer type problems ocurring on wings in which the static pressure is sensibly constant across the viscous layer. Therefore, an approach is sought which allows the static pressure to be imposed at the boundary layer edge, but which can be used in three-dimensional flows having streamwise and/or crossflow separation.

When the flow is steady and contains little or no separation, standard boundary layer prediction schemes have reached a high level of sophistication and predictive accuracy, even in three space dimensions. In unsteady flows, such as are commonly encountered in rotary winged aircraft and fixed winged aircraft at transonic speeds, some progress has been made in two space dimensions but little to date has appeared on unsteady three-dimensional boundary layers, especially for cases where negative cross flows are encountered, i.e., the spanwise component of velocity changes sign. To be of practical value, time-dependent three-dimensional boundary layer prediction schemes require high computational efficiency and transient accuracy coupled to the ability to treat arbitrary cross flow profiles. Conventional boundary layer integration schemes have developed by forward marching the streamwise velocity in the streamwise direction and simultaneously marching along the positive spanwise direction. However, in cases where there is "reverse cross flow", one must resort to specialized differencing to march a solution through such a region.

Recently, conventional boundary layer developers have applied an implicit spanwise construction to remove the restriction of only positive cross flows. Lin and Rubin (Ref. 8) in their predictor-corrector boundary region solutions for flow over a yawed cone at moderate incidence have also shown that retaining diffusion in the spanwise direction not only eliminates the problems associated with negative cross flows, but improves upon the solutions obtained by standard three-dimensional boundary layer techniques. Furthermore, with these spanwise implicit approach boundary conditions applied at the tip the flow inboard would be influenced, if required by the physics of the flow.

As a consequence of these observations, a spanwise implicit formulation (retaining spanwise diffusion) is essential for both rotary and fixed wing applications, and it can be obtained for a very modest increase in code computational labor. Based on the experience in Refs. 9 and 10, the spanwise implicit sweep only results in a moderate increase in computational effort relative to the explicit spanwise marching approach. The extension of the conventional three-dimensional boundary layer equations to allow spanwise diffusion is easily accomplished, and in view of the improved physical representation, it has been implemented in this effort.

Since the solution is being time marched, the opportunity to take a streamwise implicit sweep at roughly the same cost as the explicit sweep (forward march) does arise. If an implicit streamwise structure is adopted, then full time linearization can be utilized. That is the linearization of the nonlinear terms is performed about the known time level, rather than a known spatial marching level. As is pointed out in Ref. 10, it is easier to obtain a consistent high order accurate spatial-temporal linearization by marching in time than in space. Further, by structuring implicitly in the space marching direction, regions of axial reverse flow would not present a computational stability problem. As a result of these combined benefits an implicit structure in all three spatial directions has been employed in this effort.

Since a full 3-D spatial integration is carried out at each time step of a transient calculation, spatial accuracy plays a very important role in the overall efficiency of the numerical method. The major goal of any spatial differencing scheme is to achieve a desired level of accuracy for the mimimum number of grid points. In addition, the scheme should be able to suppress

oscillations associated with coarse grid calculations, i.e. cell Reynolds number stability condition, without overly smearing the solution; a consequence of adding excessive artificial dissipation. Such a method (QR operator), to be discussed in subsequent sections, has been developed and is described in detail in Refs. 11 and 12. The QR operator scheme permits among its many options fourth order accurate spatial approximations.

In this report the implementation of a computer code for the efficient solution of three-dimensional time-dependent viscous flows on fixed and rotary wing aircraft is described. The Linearized Block Implicit (LBI) technique of Briley and McDonald (Refs. 13 and 14) is employed in conjunction with QR operator technique to solve the present approximate form of the turbulent Navier-Stokes equations which are derived for nonorthogonal coordinates in generalized tensor form. The rationale for the choice of this approach is discussed in detail in Refs. 14 and 15.

The basic assumption made in the derivation of these equations is that the pressure does not vary normal to the shear layer, and is obtained from an inviscid analysis. Inherent in this assumption is that the shear layer is thin. Since the boundary layer remains thin over most of the wing, except perhaps near the tip, it is expected that this assumption should not limit the applicability of the present approach.

It is also assumed that for the energy equation the stagnation temperature, T_o is constant. This assumption is a good approximation for the flow fields considered as discussed in Ref. 7, and is included here only for purposes of computer run economy. In the analysis that follows, the full energy equation could equally well have been used with consequent increase in computer run time. Employing the equation of state which relates the pressure p to the velocity components u and w by an algebraic equation, the problem with T_o assumed constant can be reduced to one involving only the three velocity components, u, w and v and three equations, the streamwise and spanwise momentum equations and the continuity equation. Hence, a block-three system is considered. If the full energy equation were to be considered, a block-four system would result due to the inclusion of the temperature as an additional unknown and thus would result in an increase in computer run time.

For turbulent flows, a two-layer mixing length model is employed and its formulation in generalized tensor notation is given. A novel method is employed for solving the continuity equation in conjunction with the momentum equations. In the following, a description of the computational procedure is given including, coordinate systems, governing equations, turbulence model, and numerical technique, i.e. QR operator and Linearized Block Implicit schemes. Thereafter, the computer code is described. Following this a detailed discussion is presented of the computations conducted, and the results obtained in meeting the Phase I objectives.

Coordinate System

Since the goal of this effort is to solve for the flow over wings and rotors an understanding of the type of geometries to be considered is essential to guide the choice of the coordinate system and the structure of the computer code. The coordinate system is not only dependent upon the geometry of the wing, but also upon the approximations that are made to the governing Navier-Stokes equations. As in boundary layer theory, the present approach assumes the pressure is constant normal to the shear layer. Inherent in the assumptions is that the shear layer is thin. As pointed out by Howarth (Ref. 16) the boundary layer assumptions lead to the conditions that one coordinate direction must be normal to the body surface while the other coordinate directions must lie on the body surface. These conditions uncouple the metric data on the surface from that in the normal direction. Hence, the metric data for the surface coordinates are functions of the surface coordinates alone, while the metric data for the normal coordinate direction are functions of that coordinate alone. The choice of the surface coordinates is rather arbitrary and is based on considerations such as the ease of construction of the grid distribution on the wing surface. For example, a rectangular planform wing could be adequately described with a Cartesian coordinate system. However, for more general planforms such as a swept and tapered wing a nonorthogonal grid which conforms with the boundaries is preferred since it represents the airfoil more accurately (cf. Fig. 1).

Another consideration is the selection of a coordinate grid distribution; the major objective being the resolution of large solution

gradients. The approach taken here is to construct coordinate transformations that contain distributions for physical mesh points. In this context, the uniform mesh of computational space is simply mapped into a suitable distributed mesh in physical space. When the transformation contains the mesh point distribution, there is no need to construct the apparatus for the discrete approximation of derivatives on a nonuniform mesh. This results in a savings in both computer logic and storage.

Hence, in this work a coordinate system is chosen that conforms with the boundaries of the physical domain, i.e., the wing surface which in general will be nonorthogonal with provisions made for analytical grid transformations (Ref. 17) in each coordinate direction.

In view of the type of geometries to be considered and the assumptions made to obtain the equations, a specialized nonorthogonal coordinate system is advocated where the metric tensor which has four independent components is given by

$$g_{ij} = \begin{bmatrix} g_{11} & g_{12} & 0 \\ g_{12} & g_{22} & 0 \\ 0 & 0 & g_{33} \end{bmatrix}$$

The subscripts 1 and 2 refer to the directions on the surface of the body while subscript 3 refers to the direction normal to the body. Since the metric data in the coordinate directions on the airfoil surface are not functions of the normal direction, the metric data in a parallel surface above the body are evaluated on the body surface (Ref. 16). Furthermore, due to the use of nonorthogonal coordinates it becomes advantageous to derive the equations in general nonorthogonal coordinates employing generalized tensors. Details of the generalized tensor notation can be found in Refs. 15, 18, and 19.

An important feature of the analysis to follow is that the governing equations which are derived, under the prescribed assumptions, are invariant for any coordinate system or any grid transformation (although, of course, the physical approximations are coordinate dependent). The grid transformations are absorbed into the geometrical coefficients, leaving the equations unaltered in form. This feature allows for the construction of the

geometric data to be contained in a single subroutine with the definition of the metric data and their derivatives as input.

In Ref. 21 the geometric properties of a surface in three-dimensions are discussed and where appropriate, the generalized tensor equivalents are given. In addition, a symmetric (uncambered) NACA four-digit airfoil is considered and the pertinent geometric coefficients are presented.

Governing Equations

In the following, the governing equations are nondimensionalized as follows, x^i with respect to the characteristic length L, the velocity with respect to U_∞, density, pressure and temperature with respect to ρ_∞, $\rho_\infty U_\infty^2$ and U_∞^2/c_p respectively and time with respect to L/U_∞. The viscosity is nondimensionalized with respect to μ_∞.

Continuity Equation

$$\frac{\partial \rho}{\partial t} + \frac{1}{J}\left(J \rho u^k\right)_{,k} = 0 \tag{1}$$

where J is the Jacobian, ρ the density, and u^k is the kth contravariant velocity component

Momentum

the i-th momentum equation in the $\vec{e}_i$ direction

$$\rho\left[\frac{\partial u^i}{\partial t} + u^k u^i\big|_k\right] = -g^{ik}\left(p + \frac{2}{3}\frac{\mu}{Re}\Delta\right)_{,k} + g^{mk}\left[\frac{\mu}{Re}u^i\big|_m\right]\Big|_k + g^{mi}\left[\frac{\mu}{Re}u^k\big|_m\right]\Big|_k \tag{2}$$

where '$,_k$' denotes a partial derivative, '$|_k$' denotes a covariant derivative and g^{ik} is a component of the metric tensor and Δ is the velocity divergence.

In Ref. 21 it was pointed out that the QR Operator scheme requires that the governing equations be in quasi-linear form and that the spatial operator in a given direction operate on only one variable. For the momentum equation this requirement prevents the implicit treatment of certain diffusion terms that arise due to the curvature effects. In the usual boundary layer

approximations these explicitly treated terms would not appear in the equation since they are of order 0 ($Re^{-1/2}$) or smaller, and should, therefore, be of little consequence.

Since mixed partial derivatives are commonly treated explicitly in orthogonal coordinate systems, we do likewise in generalized nonorthogonal coordinates and extend this concept to include mixed second covariant derivatives. All other second covariant derivatives are retained as implicit. Since the pressure is specified and impressed upon the viscous layer, its specification replaces the normal momentum equation. Thus, the streamwise and spanwise momentum equations are the only two retained. A more detailed discussion of the derivation of these equations is given in Ref. 21.

Energy Equation

For the energy equation constant stagnation temperature is assumed. Neglecting the square of the normal velocity with respect to the squares of the other velocity components

$$T_o = T + \frac{1}{2}(u_p^2 + w_p^2) + \frac{g_{12}}{h_1 h_2} u_p w_p \qquad (3)$$

where u_p and w_p and the physical velocity components. These assumptions are employed here only for simplification purposes. If warranted, they can be removed and the full energy equation can be considered.

Equation of State

The equation of state assumes a perfect gas and is given by

$$P = \frac{\gamma - 1}{\gamma} \rho T \qquad (4)$$

Linearizations

The following analyses assume a set of linear partial differential equations. However, the convective part of the momentum equation and the continuity equation are nonlinear, containing terms that involve the product of density and velocity components. In order to overcome this difficulty, the procedure described in Ref. 10 is employed to linearize the aforementioned terms by Taylor series expansion about the known time level solution.

It is important to note that in the governing equations the contravariant velocity components are used. However, as noted in Ref. 22, it is advantageous to solve for the physical velocity components. Therefore, when the governing equations are subsequently cast into a form amenable to the application of the LBI scheme, they are transformed so that the physical velocity components appear.

Turbulence Model

In turbulent flow cases, the three-dimensional ensemble-averaged turbulent flow equations are considered. The approach taken here assumes an isotropic turbulent viscosity, μ_T, relating the Reynolds' stress tensor to mean flow gradients. Using Favre averaging (Ref. 23) the governing equations then are identical to the laminar equations with velocity and density being taken as mean variables and viscosity being taken as the sum of the molecular viscosity, μ, and the turbulent viscosity, μ_T.

At this point additional closure assumptions for the Reynolds stresses are required, i.e., the evaluation of μ_T. There are a variety of approaches available, from the simpler mixing length models to the more complicated one and two-equation models. Since the intention here is to verify the code's performance in wall bounded cases, the mixing length model which has worked well in the past for similar flow environments (Ref. 24) was chosen. The extension to more complex models could be undertaken at a later time if warranted. At that time, the LBI procedure that is used for the solution of the momentum equation could be applied to the kinetic energy of turbulence and the turbulent dissipation equations.

Employing the Prandtl mixing length concept, the turbulent viscosity is given as

$$\mu_T = \rho \ell^2 \sqrt{\Phi} \tag{6}$$

where ℓ is the mixing length and Φ is the dissipation function, which in generalized tensor notation is given by

$$\Phi = \frac{1}{2} e^{ij} e_{ij} \tag{7}$$

As in the Cartesian tensor formulation, Φ does not automatically reduce to the dominant term for standard boundary layers, i.e., $\partial u/\partial y$ in two dimensions and $\left((\partial u/\partial y)^2 + (\partial w/\partial y)^2\right)^{1/2}$ in three dimensions. Hence, provisions are made in the computer code that on option retains only the dominant components of the strain.

The mixing length formulation is based on McDonald's model (Ref. 25), and is given by

$$\ell = \ell_\infty \tanh\left(\frac{\kappa y}{\ell_\infty}\right) \mathcal{D} \tag{8}$$

where ℓ_∞ is the outer layer length scale and

$$\mathcal{D} = 1 - \exp(-y^+/A^+) \tag{9}$$

where y^+ takes on its usual meaning. The constants appearing in Eqs. 8 and 9, κ,λ and A^+ are .4, .09 and 26.0 respectively and δ is the local boundary layer thickness defined as .995 U_e. Note that in the limit as $y \to 0$ Eq. 8 reduces to

$$\ell_1 = k y \mathcal{D}$$

while for y large Eq. 8 reduces to

$$\ell_0 = \ell_\infty$$

the standard two layer values.

Spatial Difference Approximations

QR Operator Notation

In this section, implicit tridiagonal finite difference approximations to the first and second derivatives and to the spatial differential operator are considered. The QR operator procedure for generating a variety of spatial discretizations is also introduced. As special cases, standard second-order finite differences, first-order upwind differences, fourth-order operator compact implicit (OCI), fourth-order generalized OCI and exponential type methods are obtained. Since all these schemes are of the same form (cf. below), a single subroutine which defines the difference weights is all that is required to identify the method, while leaving the basic structure of the program unaltered. The rationale for the use of the QR approach in the present problem is discussed in detail in Ref. 14.

The QR formulation allows for ADI methods and permits the treatment of systems of coupled equations, i.e., LBI methods. Although variable mesh schemes can be employed within the QR framework, it is believed preferable to use analytic transformations to obtain a uniform computational mesh, hence attention is restricted to uniform mesh formulations.

The general concepts and notation will be introduced for two-point boundary value problems and then the methodology will be extended to more general linear and nonlinear parabolic partial differential equations in one dimension. The application of QR operator method to multidimensional problems is discussed in the section pertaining to the LBI scheme.

Consider the two-point boundary value problem

$$\tilde{L}(u) = \tilde{a}(x)u_{xx} + \tilde{b}(x)u_x + \tilde{c}(x)u = \tilde{f}(x) \tag{10}$$

with boundary values u(0) and u(1) prescribed. Derivative boundary conditions, although not discussed here, can easily be incorporated into the framework of the QR operator notation. Let the domain be discretized so that $x_j = (j-1)h$, $j = 1, 2, \ldots, J+1$, and $U_j \sim u(x_j)$, $F_j \sim u_x(x_j)$, $S_j \sim u_{xx}(x_j)$ and $h = 1/J$ is the mesh width. The numbering convention was chosen here to be compatible with FORTRAN coding.

Without loss in generality for $a(x) \neq 0$, Eq. (10) can be divided by $a(x)$ so that we may treat instead the following equation

$$L(u) = u_{xx} + b(x)u_x + c(x)u = f(x) \tag{11}$$

where

$$b(x) = \tilde{b}(x)/\tilde{a}(x),\ c(x) = \tilde{c}(x)/\tilde{a}(x) \text{ and } f(x) = \tilde{f}(x)/\tilde{a}(x)$$

Substituting the finite difference approximations to the first and second derivatives

$$\frac{D_0}{2h}U_j = \frac{U_{j+1} - U_{j-1}}{2h} = F_j = u_x(x_j) + O(h^2) \tag{12}$$

$$\frac{D_+D_-}{h^2}U_j = \frac{U_{j-1} - 2U_j + U_{j+1}}{h^2} = S_j = u_{xx}(x_j) + O(h^2) \tag{13}$$

into Eq. (11) and rearranging, we obtain

$$L(u) = \left[\frac{1}{h^2} - \frac{b_j}{2h}\right]U_{j-1} + \left[c_j - \frac{2}{h^2}\right]U_j + \left[\frac{1}{h^2} + \frac{b_j}{2h}\right]U_{j+1} = f_j \quad (14)$$

or

$$\left[1 - \frac{Rc_j}{2}\right]U_{j-1} + \left[h^2c_j - 2\right]U_j + \left[1 + \frac{Rc_j}{2}\right]U_{j+1} = h^2f_j \quad (15)$$

where $Rc_j = hb_j$ is the cell Reynolds number.

Equation (15) can be generalized by introducing operator format, i.e.,

$$r_j^- U_{j-1} + r_j^c U_j + r_j^+ U_{j+1} = h^2(q_j^- f_{j-1} + q_j^c f_j + q_j^+ f_{j+1}) \quad (16)$$

where the superscripts (-) minus, (c) center, and (+) plus indicate the difference weight that multiplies the variable evaluated at the (j-1), (j) and (J+1) grid points respectively, and where the r_j's and q_j's for grid point j are functions of h, b_{j-1}, b_j, b_{j+1}, c_{j-1}, c_j and c_{j+1}.
Comparing Eqs. (15) and (16) we can identify the r_j's and q_j's, viz.,

$$\begin{aligned} r_j^- &= 1 - Rc_j/2 & q_j^- &= 0 \\ r_j^c &= h^2c_j - 2 & q_j^c &= 1 \\ r_j^+ &= 1 + Rc_j/2 & q_j^+ &= 0 \end{aligned} \quad (17)$$

We now define the tridiagonal difference operators Q and R

$$\begin{aligned} R[U_j] &= r_j^- U_{j-1} + r_j^c U_j + r_j^+ U_{j+1} \\ Q[f_j] &= q_j^- f_{j-1} + q_j^c f_j + q_j^+ f_{j+1} \end{aligned} \quad (18)$$

Noting that L(u) = f and substituting Eq. (18) into Eq. (16), we obtain

$$R[U_j] = h^2Q[f_j] = h^2Q[L(u)_j] \quad (19)$$

Alternatively by employing the inverse operator Q^{-1} an expression for $L(u)_j$ can be obtained

$$L(u)_j = \frac{1}{h^2} Q^{-1} R U_j \tag{20}$$

For standard central finite differences $Q = Q^{-1} = I$, the identity matrix, so the spatial operator can be given explicitly in terms of U_{j-1}, U_j and U_{j+1}. However, in general, for higher order methods whereas Q is tridiagonal Q^{-1} is a full matrix, and the spatial operator cannot be given explicitly in terms of the variables at adjacent grid points. Hence, Eq. (20) provides a method for expressing the spatial operator for a wider class of difference approximations. The formalism in Eq. (20) is also applicable for first and second derivatives appearing alone (cf. Ref. 11). In Refs. 12 and 14 a technique due to Berger, et al is described for constructing fourth order tridiagonal methods which possess a monotonicity property as the cell Reynolds number is increased, $R_c \to \infty$. This type of scheme is an option in the computer code.

Application to Coupled Nonlinear Parabolic Equations

Before considering the LBI technique, we discuss some of the limitations placed on the QR operator scheme in solving a system of nonlinear parabolic equations.

Given a system of m nonlinear parabolic equations in m unknowns,

$$\sum_{i=1}^{m} \left\{ \frac{1}{a_{ij}^{n+\beta}} \frac{(u_{ij}^{n+1} - u_{ij}^{n})}{\Delta t} - N_i^{n+\beta}(u_1, u_2, \ldots u_m, x_1, x_2, x_3, t) \right\} = 0$$

$$j = 1, 2, \ldots, J+1$$

where $N_i^{n+\beta}$ is a quasilinear spatial operator, the QR formalism carries directly over provided that for any equation only one independent variable is operated upon by the differential operator. For example,

$$\frac{1}{a(u,w,v)} u_t = u_{xx} + b(u,v,w)u_x + c(u,v,w)$$

is allowed since x derivatives of u only appear, while

$$\frac{1}{a(u,w,v)}\, u_t = u_{xx} + b(u,v,w)u_x + c(u,v,w) + d(u,v,w)w_x$$

is not allowed since x derivatives of both u and w appear. The approximate form of the unsteady Navier-Stokes equations used here, when written in quasi-linear form, falls within the class of allowable differential operators. Thus, for the problem being addressed in the present study, the OCI schemes are applicable. Note that within the splitting approach, nonallowable terms in the OCI scheme such as dw_x above, may be split off and treated by a special implicit sweep. Provided care is taken and for instance the Douglas-Gunn (Ref. 26) formalism is adhered to, no particular problem arises other than the cost of an additional implicit sweep which is incurred.

Thus, multidimensional problems and/or more general equation forms can usually be accommodated by a splitting procedure, which reduces the differential operator to a sequence of one-dimensional problems which have the appropriate allowable form. However, as with standard finite differences, to avoid the cost of additional implicit sweeps, special procedures must be applied to cross derivative terms, e.g., extrapolation or explicit treatment.

Linearized Block Implicit Scheme

Consider a system of nonlinear partial differential equations

$$A\vec{\Phi}_t = \mathcal{D}\vec{\Phi} + \vec{\Psi} \tag{21}$$

where $\vec{\Phi}$ is a vector of unknowns and Ψ is a source term vector which is a function of x^1, x^2, x^3 and t. Extension to source terms which are functions of $\vec{\Phi}$ are discussed in Ref. (10). $\mathcal{D}$ is a three-dimensional nonlinear differential operator and the matrix A appearing in the momentum equations is equal to ρI where ρ is the density and I the unity matrix.

Equation (21) may be centered about the $n+\beta$ time level, i.e. $t^{n+\beta} = (n+\beta)\Delta t = n\Delta t + \beta\Delta t = t^n + \beta\Delta t$, and written

$$A^{n+\beta}\left[\vec{\Phi}^{n+1} - \vec{\Phi}^n\right]/\Delta t = \mathcal{D}^{n+\beta}\vec{\Phi}^{n+\beta} + \vec{\Psi}^{n+\beta} \tag{22}$$

where $0 \leq \beta \leq 1$ is a parameter allowing one to center the time step, i.e., $\beta = 0$ corresponds to a forward difference, $\beta = 1/2$ to Crank-Nicolson and $\beta = 1$ to a backard difference.

After linearizing Eq. (22) by Taylor series expansion in time about the n^{th} time level by the procedure described in Ref. 10 to give a second-order linearization, we obtain

$$A^n\left[\bar{\Phi}^{n+1} - \bar{\Phi}^n\right]/\Delta t = \mathcal{L}^n\left[\bar{\Phi}^{n+\beta} - \bar{\Phi}^n\right] - \mathcal{D}^n\bar{\Phi}^n + \bar{\Psi}^{n+\beta} \tag{23}$$

where $\mathcal{L}$ is the linearized differential operator obtained from $\mathcal{D}$.

The difference between the nonlinear operator $\mathcal{D}$ and the linear operator $\mathcal{L}$ is defined as $M^n = \mathcal{D}^n - \mathcal{L}^n$. At the intermediate level $n + \beta$, $\Phi^{n+\beta}$ is represented as

$$\bar{\Phi}^{n+\beta} = \beta\,\bar{\Phi}^{n+1} + (1-\beta)\bar{\Phi}^n \tag{24}$$

Using these relationships and dropping the vector superbar for convenience a two-level hybrid implicit-explicit scheme is obtained

$$A^n(\Phi^{n+1} - \Phi^n)/\Delta t = \beta\mathcal{L}^n(\Phi^{n+1} - \Phi^n) + \mathcal{L}^n\Phi^n + M^n\Phi^n + \Psi^{n+\beta} \tag{25}$$

The vector $\psi^{n+\beta}$ represents all of the terms in the system of equations which are treated explicitly. More about this will be said later, but for the moment note that $\psi^{n+\beta}$ may be approximated to the requisite order of accuracy by some multilevel linear explicit relationship, or approximated by ψ^n with a consequent order reduction in temporal accuracy.

The operator $\mathcal{L}$ is now expressed as a sum of convenient, easily invertible suboperators $\mathcal{L} = \mathcal{L}_1 + \mathcal{L}_2 + \ldots . \mathcal{L}_m$. In the usual ADI framework these suboperators are associated with a specific coordinate direction. Further, it is supposed that these suboperators can be expressed in the QR notation introduced earlier. Writing $\psi^{n+\beta}$ and $M^n\Phi^n$ as a single source term $S^{n+\beta}$, Eq. (25) is written as

$$A^n\left[\Phi^{n+1} - \Phi^n\right]/\Delta t = \beta\left[\mathcal{L}_1^n + \mathcal{L}_2^n + \mathcal{L}_3^n\right]\left[\Phi^{n+1} - \Phi^n\right] + \left[\mathcal{L}_1^n + \mathcal{L}_2^n + \mathcal{L}_3^n\right]\Phi^n + S^{n+\beta} \tag{26}$$

To solve this system efficiently it is split into a sequence of easily invertible operations following a generalization of the procedure of Douglas and Gunn (Ref. 26) in its natural extension to systems of partial differential equations. The Douglas-Gunn splitting of Eq. (26) is written as the following three-step procedure

$$
\begin{aligned}
A^n\left[\Phi^* - \Phi^n\right]/\Delta t &= \beta \mathcal{L}_1^n(\Phi^* - \Phi^n) + \left[\mathcal{L}_1^n + \mathcal{L}_2^n + \mathcal{L}_3^n\right]\Phi^n + S^{n+\beta} \\
A^n\left[\Phi^{**} - \Phi^n\right]/\Delta t &= \beta \mathcal{L}_1^n\left[\Phi^* - \Phi^n\right] + \beta \mathcal{L}_2^n\left[\Phi^{**} - \Phi^n\right] + \left[\mathcal{L}_1^n + \mathcal{L}_2^n + \mathcal{L}_3^n\right]\Phi^n + S^{n+\beta} \\
A^n\left[\Phi^{***} - \Phi^n\right]/\Delta t &= \beta \mathcal{L}_1^n\left[\Phi^* - \Phi^n\right] + \beta \mathcal{L}_2^n\left[\Phi^{**} - \Phi^n\right] + \beta \mathcal{L}_3^n\left[\Phi^{***} - \Phi^n\right] \\
&\quad + \left[\mathcal{L}_1^n + \mathcal{L}_2^n + \mathcal{L}_3^n\right]\Phi^n + S^{n+\beta}
\end{aligned}
\tag{27}
$$

which can be transformed to the alternative form

$$
\begin{aligned}
\left[A^n - \Delta t \beta \mathcal{L}_1^n\right]\left[\Phi^* - \Phi^n\right] &= \Delta t\left[\mathcal{L}_1^n + \mathcal{L}_2^n + \mathcal{L}_3^n\right]\Phi^n + \Delta t S^{n+\beta} \\
\left[A^n - \Delta t \beta \mathcal{L}_2^n\right]\left[\Phi^{**} - \Phi^n\right] &= A^n\left[\Phi^* - \Phi^n\right] \\
\left[A^n - \Delta t \beta \mathcal{L}_3^n\right]\left[\Phi^{***} - \Phi^n\right] &= A^n\left[\Phi^{**} - \Phi^n\right]
\end{aligned}
\tag{28}
$$

If the intermediate levels are eliminated, the scheme can be written in the so-called factored form

$$
\begin{aligned}
&(A^n - \beta \Delta t \mathcal{L}_1^n)(A^n)^{-1}(A^n - \beta \Delta t \mathcal{L}_2^n)(A^n)^{-1}(A^n - \beta \Delta t \mathcal{L}_3^n)(\Phi^{n+1} - \Phi^n) = \\
&\qquad \Delta t(\mathcal{L}_1^n + \mathcal{L}_2^n + \mathcal{L}_3^n)\Phi^n + \Delta t S^{n+\beta}
\end{aligned}
\tag{29}
$$

The ADI formulation given in Eq. (28) is directly applicable for $\mathcal{L}_i$ operators represented in $Q^{-1}R$ operator format. Consideration of intermediate boundary conditions and the removal of the inverse operator Q^{-1} is given in Ref. 21.

It is worth noting that the operator $\mathcal{D}$ or $\mathcal{L}$ can be split into any number of components which need not be associated with a particular coordinate direction. As pointed out by Douglas and Gunn (Ref. 26), the criterion for identifying sub-operators is that the associated matrices be "easily solved" (i.e., narrow-banded). Thus, mixed derivatives and

complicating terms which might inhibit the use of OCI can be treated implicitly within such a framework, although this would increase the number of intermediate steps and thereby complicate the solution procedure.

An inspection of Eq. (28) reveals that only the linearized operators $\mathcal{L}_1^n$, $\mathcal{L}_2^n$ and $\mathcal{L}_3^n$ appear. Indeed, the computer code employs this feature by evaluating these three operators before the first sweep, storing them and accessing them as needed in the subsequent three sweeps. In addition, the terms arising from the nonlinear terms are immediately absorbed into $S^{n+\beta}$ as they appear, allowing for an efficient evaluation of the terms in the differential equations.

The spatial operators appearing in the differential equations $\mathcal{L}_1^n$, $\mathcal{L}_2^n$ and $\mathcal{L}_3^n$ must be identified at least formally in order to isolate the coefficients that are to be used in the construction of the Q and R operators. These operators can be represented in standard form at each grid point, i.e.,

$$\mathcal{L}_1^n \Phi_1^n = a_{11}^n \Phi_{1,11} + a_{12}^n \Phi_{1,1} + a_{13}^n \Phi_1 + a_{14}^n \Phi_2 + a_{15}^n \Phi_3 \qquad (30)$$

In Eq. (30) the first subscript of Φ indicates the velocity component (associated with the corresponding direction) and " , " indicates a derivative. The subscripts of the a_{ij}^n refer to the direction (i) and the term in the equation (j) respectively. Note that the equation is in quasi-linear form, since the coefficients of the derivative operators need to be identified, for use with the QR operator technique employed here. Alternate schemes have been proposed by Leventhal (Ref. 27) for equations in conservation form but are not considered here. In the following section, a description will be given of how this entire operator is discretized by employing the QR operator format, and how the discretization is incorporated into the LBI framework in order to solve the system of equations (28).

The continuity equation is considered first. Since it is a first-order partial differential equation it does not have the standard form of Eq. (29). Furthermore, in the linearization process ρ has been eliminated in favor of the u^i velocity components so that the continuity equation has become an equation for the three velocity components, and not density.

An inspection of the system of equations under consideration reveals that substantial savings can be realized if the equations are partioned appropriately. Since the normal to the body ("3" direction) momentum equation is not solved, the normal velocity appears only in conjunction with terms associated with the normal "3" direction in the other two momentum equations. Hence, in the first two sweeps where directions "1" and "2" are implicit one is required to solve only for the two corresponding velocity components in the streamwise and spanwise momentum equation without the need of considering the continuityequation. However, on the third sweep where all 3 velocity components appear, one must solve all 3 equations. This strategy reduces the solution procedure to the inversion of two 2 × 2 block matrices and one 3 × 3 block matrix rather than three 3 x 3 block matrices which leads to a substantial reduction in computation time. If the full Navier-Stokes equations were considered (including a normal momentum equation) the aforementioned partioning could not be applied since the normal velocity would appear in all three sweeps.

The question that arises is how to appropriately split the continuity equation, since it need only be solved on the third sweep. Here again the Douglas-Gunn formulation leads to the appropriate choice. The continuity equations written in conservation form is,

$$\frac{\partial \rho}{\partial t} + \frac{1}{J} \frac{\partial}{\partial x^1} \left[J \rho u^1 \right] = 0 \tag{31}$$

After linearizing and eliminating ρ, the increment form is obtained

$$\begin{aligned} A^n \Delta u^{n+1} + B^n \Delta W^{n+1} + \frac{\Delta t \beta}{J} \frac{\partial}{\partial x^3} \left[v^n A^n \Delta u^{n+1} + v^n B^n \Delta w^{n+1} + \rho^n \Delta v^{n+1} \right] \\ = - \frac{\Delta t}{J} \frac{\partial}{\partial x^1} \left[J \rho u^1 \right]^n + \frac{\Delta t \beta}{J} \frac{\partial}{\partial x^1} \left[(\rho^n + u^n A^n) \Delta u^{n+1} + (u^n B^n) \Delta w^{n+1} \right] \\ + \frac{\Delta t \beta}{J} \frac{\partial}{\partial x^2} \left[(\rho^n + w^n B^n) \Delta w^{n+1} + (w^n A^n) \Delta u^{n+1} \right] \end{aligned} \tag{32}$$

where all the velocity components are the contravariant components $u = u^1$, $w = u^2$ and $v = v^3$. J is the Jacobian and

$$A^n = \frac{\rho^n}{T^n}\left[g_{11}u^n + g_{12}w^n\right]$$

$$B^n = \frac{\rho^n}{T^n}\left[g_{22}w^n + g_{12}u^n\right]$$

By employing the Douglas-Gunn procedure, Eq. (32) is represented as a third sweep equation, and a consistent approximation is obtained to the continuity equation, i.e., the x^1 derivative term is evaluated at the * level and the x^2 derivative term is evaluated at the ** level. The values of the intermediate derivative terms are obtained after the solution of the first two sweeps of the two momentum equations. Note that these terms do not contain the normal velocity. The equation can thus be written in symbolic form

$$A^n\Delta u^{n+1} + B^n\Delta w^{n+1} + \frac{\Delta t\beta}{J}\frac{\partial}{\partial x^3}\left[J\left\{A^n v^n\Delta u^{n+1} + v^n B^n\Delta w^{n+1} + \rho^n\Delta v^{n+1}\right\}\right] \tag{33}$$

$$= S^n - \beta\frac{\Delta t}{J}\frac{\partial}{\partial x^1}\left[J\{\ \}\right]^* - \beta\frac{\Delta t}{J}\frac{\partial}{\partial x^2}\left[J\{\ \}\right]^{**}$$

Since the only term involving v is in the x^3 derivative term, one can directly integrate the equation with respect to x^3, i.e.

$$\int_{x^3}\left[A^n\Delta u^{n+1} + B^n\Delta w^{n+1}\right]dx^3 + \Delta t\frac{\beta\Delta t}{J}\left[v^n A^n\Delta u^{n+1} + v^n B^n\Delta w^{n+1} + \rho^n\Delta v^{n+1}\right]$$

$$= \int_{x^3}\left\{S^n - \frac{\beta\Delta t}{J}\left[\ \right]^* - \frac{\beta\Delta t}{J}\left[\ \right]^{**}\right\}dx^3$$

The next section describes how this is done very easily via the QR operator scheme. The concept of integrating directly the continuity equation is not new. Blottner (Ref. 28) attributes a similar coupled procedure to Davis for the two-dimensional steady boundary layer equations in which the trapezoidal rule is used to integrate the continuity equation. Weinberg (Refs. 29 and 30) also used a fourth-order Simpson integration scheme to solve the compressible boundary layer equations. Such procedures are stable and offer a viable alternative to approximating the derivatives by finite differences. Note that conceptually the continuity equation in integrated form is treated

on each sweep of the Douglas-Gunn splitting, although in actuality the continuity equation is solved only on the third sweep. The stability and consistency of the original splitting is still retained since the split integration operators can be incorporated into the $\mathcal{L}$ and $\mathcal{D}$ difference operators (cf. Eqs. 27 and 28).

Implementation of the LBI Scheme Employing the QR Operator Technique

Consider the third sweep of Eq. (27) in which both momentum equations and the continuity equation are solved. The momentum equations are in the form

$$\left[A^n - \beta\Delta t\mathcal{L}_3^n\right]\Delta\Phi^{***} = A^n\Delta\Phi^{**} \tag{34}$$

where $\Delta\Phi^{***}$ is the column vector of unknowns, u, v, w. Here it has been implicitly assumed that the equations have been appropriately normalized and that the contravariant velocity components have been suitably transformed into their physical components. Employing physical components, (cf. Ref. 22) leads to a better behaved solution since these components are not unduly influenced by geometrical variations.

For the streamwise momentum equation one obtains

$$\mathcal{L}_3^n\,\Delta\Phi^{***} = \Delta u_{,33} + u_{23}\,\Delta u_{,3} + a_{33}\Delta u + a_{43}\Delta w + a_{53}\Delta v \tag{35a}$$

while for the spanwise momentum equation one obtains

$$\mathcal{L}_3^n\Delta\Phi^{***} = \Delta w_{,33} + b_{23}\Delta w_{,3} + b_{33}\Delta w + b_{43}\Delta v + b_{53}\Delta u \tag{35b}$$

where superscript *** has been omitted from Δu, Δv and Δw. Now in Eq. (35a), the first three terms on the right-hand side are approximated by the operator equivalent so that

$$\mathcal{L}_3^n\,\Delta\Phi^{***} = \frac{Q_1^{-1}R_1\Delta u}{\Delta x_3^2} + a_{43}\Delta w + a_{53}\Delta v \tag{36}$$

Similar approximations are made for Eq. (35b). After substituting Eq. (36) into Eq. (34), and multiplying through by Q, one obtains for the streamwise momentum equation

$$\left[Q_1 \rho^n - \beta \lambda R_1\right] \Delta u - \beta \Delta t Q_1 a_{43} \Delta w - \beta \Delta t Q_1 a_{53} \Delta v = Q_1 \rho^n \Delta u^{**} \qquad (37)$$

where $\lambda = \Delta t / \Delta x_3^2$. A similar expression is obtained for the spanwise momentum equation.

The same type of procedure is also employed for the continuity equation. Since the continuity equation involves only first derivatives, they can be represented as

$$\frac{\partial}{\partial x^3} = \frac{Q_c^{-1} R_c}{\Delta x_3} \qquad (38)$$

were Qc and Rc are the QR operators associated with the continuity equation. The operators Qc and Rc are constructed to approximate the weights associated with either a second-order trapezoidal rule or a fourth-order Simpson's rule, i.e.,

Trapezoidal rule

$$q_c^- = 0 \ , \ q_c^c = \frac{1}{2} \ , \ q_c^+ = \frac{1}{2}$$

$$r_c^- = 0 \ , \ r_c^c = -1 \ , \ r_c^+ = 1$$

Simpson's rule

$$q_c^- = \frac{1}{3} \ , \ q_c^c = \frac{4}{3} \ , \ q_c^+ = \frac{1}{3}$$

$$r_c^- = -1 \ , \ r_c^c = 0 \ , \ r_c^+ = 1$$

The discretized continuity equation thus becomes after multiplying thru by Q_c

$$\left[Q_c J A^n + \beta\omega R_c J A^n v^n\right]\Delta u + \left[Q_c J B^n + \beta\omega R_c J B^n v^n\right]\Delta w + \left[\beta\omega R_c J \rho^n\right]\Delta V = Q_c(RHS) \quad (39)$$

where RHS contains all the terms due to the linearization procedure and the terms evaluated at the * and ** levels and $\omega = \Delta t/\Delta x_3$. The resulting matrix derived from Eqs. (37) and (39) becomes a block 3 tridiagonal matrix (Q_1, R_1, Q_2, R_2, Qc and Rc are tridiagonal operators) with each sub block taking the form

$$\begin{bmatrix} \left[\quad Q_1\rho^n - \beta\lambda R_1 \quad\right] & \left[\quad -\beta\Delta t\, Q_1 a_{43} \quad\right] & \left[-\beta\Delta t Q_1 a_{53}\right] \\ \left[\quad -\beta\Delta t\, Q_2 b_{53} \quad\right] & \left[\quad Q_2\rho^n - \beta\lambda R_2 \quad\right] & \left[-\beta\Delta t Q_2 b_{43}\right] \\ \left[Q_c J A^n + \beta\omega R_c J A^n v^n\right] & \left[Q_c J B^n + \beta\omega R_c J B^n v^n\right] & \left[\beta\omega R_c J \rho^n\right] \end{bmatrix} \begin{bmatrix} \Delta u \\ \Delta w \\ \Delta v \end{bmatrix} = \begin{bmatrix} Q_1(\Delta u^{**}) \\ Q_2(\Delta w^{**}) \\ Q_c(RHS) \end{bmatrix}$$

The matrix is inverted by standard LU decomposition.

The Computer Code

The type of numerical algorithm employed as well as its formulation has a marked impact on the structure of the computer code. One needs to consider both the number of CPU operations as well as the memory requirements. Usually, the number of operations can be reduced at the expense of increasing the amount of storage. For the type of problems under consideration both in two and three dimensions, with their large data bases, core requirements be-

come a stringent constraint and external disk storage must be employed. An additional consideration is the allocation and acquisition of data, in particular how this impacts upon code vectorization. With these requirements in mind the code has been structured in such a way as to exploit available core and disk files by employing concurrent data transfer (buffer type statements) and structuring the code to operate on lines of data so that vectorization is possible. The calculations that are discussed in the next section were obtained on the CRAY 1 computer situated at the University of Minnesota computer center. The original version of the code was developed to run efficiently on a CDC 7600 scaler machine. That version was transferred to the CRAY, but was not modified to exploit the vectorization capabilities of the machine since that was not within the scope of the present contract. Hence, the quoted run times, which are low, could still be reduced substantially if full vectorization is taken into account. This could be part of a Phase II effort. However, certain features have been incorporated into the code which leads to the mentioned efficient run times. The modifications described above are suitable for other vector processers such as the CYBER 205 as well as the CRAY.

An investigation of the operation count of the LBI scheme in conjunction with the QR operator technique reveals that the most significant fraction of time is spent in computing the matrix coefficients, i.e. the linearization coefficients and difference weights, and exceeds the time required for the matrix inversions. Hence, it is worthwhile to optimize the calculation of these coefficients, and if possible store their values. This was accomplished by storing the operator coefficients $\mathcal{L}_2^n$ and $\mathcal{L}_3^n$ as they were computed in the first sweep on the right-hand side of the differential equation. On the second and third sweeps $\mathcal{L}_2^n$ and $\mathcal{L}_3^n$ were accessed respectively and were not recomputed. It was for this reason that the formulation of the LBI scheme referred to the linearized operators $\mathcal{L}_i^n$'s instead of the $\mathcal{D}_i^n$'s on the right-hand side of the equation.

The general structure of the computer code will now be described. After the input section and the initialization of data e.g. geometry, grid transformations, initial flowfield, etc. the actual construction of the difference operators is begun. The first derivatives of the velocity components and viscosity are obtained for the entire flow field and stored for ready access when needed for the computation of the appropriate terms in

the governing equations. Thereafter the terms that are to be treated explicitly are evaluated and absorbed into the function S^n.

The operators $\mathcal{L}_1$, $\mathcal{L}_2$ and $\mathcal{L}_3$ are then computed. These are used to evaluate the appropriate Q and R coefficients which are then stored for easy retrieval during each of the ADI sweeps.

In the first sweep the matrix resulting from the application of the $\mathcal{L}_1$ operators for the streamwise and spanwise momentum equation is solved as a 2 × 2 coupled system. The solution of this system, the * level quantities, are then used to construct the right-hand side of the second sweep equations and to evaluate the appropriate * level term in the continuity equation. At this point the $\mathcal{L}_2$ operator is accessed and again a 2 × 2 system of equations for the streamwise and spanwise momentum equation is solved. The ** level quantities are then used to construct the right-hand side of the third sweep equations as well as the appropriate terms in the continuity equation. For the third sweep equations which consist of the two momentum equations and the continuity equation, the $\mathcal{L}_3$ operator is accessed from memory. The resulting 3 × 3 system of equations is solved for the three velocity components.

After the primary variables are evaluated, the thermodynamic quantities, density, temperature and viscosity are computed. The procedure is then repeated at the following time steps.

Discussion of Results

In order to validate the numerical procedure for solving the three-dimensional unsteady turbulent approximate form of the Navier-Stokes equations it is necessaary to compare with available experimental data. Unfortunately, reliable three-dimensional data is rare and it is necessary to resort to alternate strategies in order to achieve this goal. Previously one of the present authors has successfully employed a procedure for verifying the numerical method for three-dimensional steady laminar flow (cf Ref. 14). A three-dimensional flow field was derived from a two-dimensional one by performing a coordinate rotation of the computational domain through a specified angle (for instance 45°) as shown in Fig. 2. As can be seen in Fig. 2 this is analogous to considering a uniform flow over a flat plate skewed at the rotation angle. In the orthogonal coordinate system consisting

of the leading edge of the plate and the normal to it (ξ,ζ) the flow is two-dimensional. However, when viewed in the x^1, x^2 coordinate system the flow is a restricted type of three-dimensional flow involving in addition to the streamwise and normal velocities a spanwise component. Although this represents a restricted three-dimensional flow, it serves as a valid three-dimensional test case for the code.

Such a procedure has several attractions over considering an actual three-dimensional flow. First, the analogous two-dimensional calculation (in the ξ,ζ coordinate system) can be performed giving additional information with which verifications can be made to assess proper code operation in the thee-dimensional mode. Second, three-dimensional geometrical effects are removed allowing for a more direct comparison of the numerical results with the data. Third, turbulence modeling is simplified since the models have, in effect, no three-dimensional complications other than the contribution to the dissipation appearing in the mixing length formulation (cf Eq. 6). Finally, the two-dimensional calculation can facilitate the validation of the three-dimensional calculation.

Having resolved the three-dimensional problem to be considered, the remaining task reduces to determining the appropriate two-dimensional experimental case with which comparisons are to be made. In recent years there has been great interest in the experiments of Karlsson (Ref. 31). Karlsson conducted a set of experiments for a zero pressure gradient flat plate flow whose external velocity consisted of sinusoidal fluctuations superimposed upon a mean velocity, i.e.,

$$u = u_0(1 + A\cos\omega t) \tag{40}$$

where A is the amplitude of the oscillations and ω is its circular frequency. The magnitude of the amplitude ranged from 8% to 34%, while the oscillation frequency ranged from 0 to 48 Hz. Karlsson measured the mean velocity, the in phase and out of phase components of the first harmonic of the periodic fluctuations as well as the sum of the turbulent intensity and the contribution of the higher harmonics. A schematic of this test facility reproduced from a report by Carr (Ref. 32) is shown in Fig. 3 , and consists of a rectangular tunnel with the unsteady fluctuations being introduced by a rotating shutter assembly at the exit of the tunnel.

In Fig. 4 are shown recent computational results that have been obtained for the phase angle lead of the skin friction (cf. Refs. 32, 33, 34, 35, and 36). The phase angle of the first harmonic of the skin friction is plotted against the reduced frequency, $\omega x/u_o$. It is immediately apparent that there is a wide variation in the predicted results. For laminar flow there is a direct correlation between the phase angle and the reduced frequency. As can be seen in Fig. 5 (cf. Ref. 21), the phase angle approaches an asymptote of 45° corresponding to Lighthill's high frequency limit (Ref. 37) for large values of the reduced frequency. For turbulent flow, as shown in Fig. 4, there does not appear to be this direct correlation nor does the data approach an asymptotic value as observed for the laminar case. Such an asymptotic behavior would be plausible from physical consideration since the skin friction is dependent on the local flow properties near the wall, i.e. viscous sublayer. Furthermore, there does not appear to be any correspondence among the various predictions. An explanation for some of these disparaties is proposed and will be discussed below. For the moment it must be kept in mind that the experiments conducted by Karlsson are more than 25 years old and the methods used for obtaining and reducing the data were not as sophisticated nor as reliable as they are today. More disturbing from a computational point of view is that there is data at only one streamwise location and there is no upstream data with which to make comparisons. Another concern is the low Reynolds number, approximately 10^5/ft at which the experiment was conducted. However, the the experimental data remains valuable and can be used to verify calculation procedures.

In calculating this flow it was intended to be as faithful as possible to the actual flow conditions of the experiment. This could not be totally achieved due to the low Reynolds number of the experiments which would necessitate the consideration of unsteady transition, and the inclusion of low Reynolds number effects. Since this was not within the scope of the present effort, fully turbulent conditions were assumed. Hence, at the upstream boundary the velocity profile employed was a fully turbulent one. This is in contrast to some other numerical predictive methods in which it is assumed that the laminar flow developing from the leading edge of a flat plate undergoes instantaneous transition to turbulent flow at some predetermined streamwise location.

In view of the lack of upstream information and the low Reynolds number, the determination of a physical streamwise location for the upstream boundary required some attention. The experimental data of Wieghardt (Ref. 38) in conjunction with the curve fits of Clauser (Ref. 39) were the starting points for determining the upstream profile as well as the physical streamwise extents of the computational domain. In Fig. 6 Wieghardt's data is plotted in c_f, $Re_{\delta*}$ coordinates along with Clauser's predictions. As can readily be seen the experimental data compares well with Clauser's predictions for $Re_{\delta*} > 2000$, but diverges from Clauser's prediction at lower values of $Re_{\delta*}$ where low Reynolds number effects are prevalent. For the present calculations, the upstream boundary was placed sufficiently far upstream of the measuring station (nominally $Re_{\delta*} = 3600$) where the numerical predictions are to be compared to the experimental data. This location was chosen to be approximately $Re_{\delta*} = 850$, with the corresponding value of $c_f = .00051$. In Fig. 6 this point lies between the Clauser curve and Wieghardt's data. Modifying these values by as much as 10% had little effect on the computed solution for $Re_{\delta*} > 1500$.

The upstream velocity profiles, which must be prescribed in the numerical computation were obtained from Cole's wall-wake law, (Ref. 38),

$$\left.\begin{aligned} \frac{u}{u_\tau} &= \frac{1}{\kappa}\ln\left(\frac{y u_\tau}{\upsilon}\right) + C + \frac{2\Pi(x)}{\kappa}\sin^2\left(\frac{\pi}{2}\frac{y}{\delta}\right) && \text{Wall-Wake Law} \\ y^+ &= u^+ && \text{laminar sublayer} \end{aligned}\right\} \qquad (41)$$

where

$$y^+ = \frac{y u_\tau}{\upsilon}, \quad u^+ = \frac{u}{u_\tau} \qquad u_\tau = \sqrt{\tau_w/\rho}$$

and $\Pi(x)/\kappa$ is evaluated from the condition that $u = u_\infty$ at $y/\delta = 1$. In Eq. (41) the constants κ and C are set at .41 and 5.0 respectively. This leaves two free parameters τ_w (or C_f) and δ, which must be chosen to completely specify the profile. Since $Re_{\delta*}$ is to be specified instead of δ an additional relationship is required. In Ref. 38 a relationship relating $Re_{\delta*}$, δ, C_f and $\Pi(x)$ is given

$$\frac{\kappa(Re_{\delta*} - 65)}{\delta u_\tau/\nu} = 1 + \Pi(x) \qquad (42)$$

Combining Eq. 41 and 42 $\Pi(x)$ can be eliminated and a transcendental equation for $\lambda = \delta u_\tau/\nu$ is obtained (with C_f and Re_{δ^*} being specified constants),

$$\frac{\overline{u_\infty}}{u_\tau} = \frac{1}{\kappa} \ln\lambda + \frac{2}{\lambda}(Re_{\delta^*} - 65) - \frac{2}{\kappa} \tag{43}$$

which can be solved for λ and hence δ by a Newton iteration procedure. In general, only two or three iterations are required for convergence. Thereafter δ and C_f are substituted in Eq. (41) to obtain the required velocity profile. In some cases the δ and C_f obtained from the iteration procedure were used as input for Musker's profile (Ref. 40). The advantage of this profile is that there is a smooth transition between the laminar sublayer and the logarithmic portion of the boundary layer.

Streamwise locations for the upstream and downstream boundaries were chosen consistent with the boundary layer properties at these locations. This was done in order to present the unsteady data as a function of $\omega x/u_o$, the reduced frequency. However, the x value so determined will not necessarily correspond to the x locations in Karlsson's experiment due to virtual origin effects which are consequences of upstream history. A correlation between C_f and Re_x was employed, to obtain these locations. The correlation which assumes a 1/7th power law profile for the velocity is given by

$$C_f = 0.0592\left(\frac{u_\infty x}{\nu}\right)^{-\frac{1}{5}}$$

Consequently, in order to obtain a Re_{δ^*} in excess of 4000 at the downstream boundary, the extent of the computational domain in the streamwise direction was set as .594 m $\leq$ x $\leq$ 4.862 m (1.95 ft $\leq$ x $\leq$ 15.95 ft).

In the normal to the wall direction, the outer boundary was chosen so that during the oscillatory motion the boundary layer edge would lie totally within the computational domain. Hence, the outer edge was placed at a nominal height of x_3 = 13.716 cm (.45 ft). In the normal direction either 41 or 51 grid points were employed. For the 41 point grid a clustering transformation of the hyperbolic tangent type was used, with the first grid point being located at x_3 = .003888 cm (.000324 ft) or y^+ = 1.407 at the upstream boundary. For the 51 point calculation Oh's transformation (Ref. 41) was used, which relies upon an error function series for the grid

clustering. The first grid point was located at x_3 = .005732 cm (.000188 ft) or y^+ = 1.0377. There were 36 uniformly spaced grid points in the streamwise direction yielding a mesh spacing of Δx_1 = 12.192 cm (.40 ft) and corresponds to nearly six boundary layer thicknesses as measured at the upstream station.

For the quasi-steady state case in order to correspond to the experimental data the Reynolds number per unit length was, R_e = 307,579/m (93,750/ft) where U_∞ = 4.572 m/sec (15 ft/sec) and ν = .0000149 sec/m^2 (.00016 sec/ft^2). For the other cases, the Reynolds number per unit length was Re = 358,842/m (109,375/ft) where U_∞ = 5.334 m/sec (17.5 ft/sec). The mesh employed in the calculation consisted of 51 x 36 = 1836 grid points. The calculation reached a steady state in 42 time steps, defined as the point at which the dependent variables u^1 and u^3 do not change by more than ε = 10^{-5} over two successive time steps. In obtaining the steady state, the solution is advanced in time from some initial guess, and the time steps are chosen in order to hasten convergence.

A comparison between the predicted mean velocity profile at x = 4.252 m (13.95 ft) corresponding to (Re_{δ^*} = 3551 and C_f = .00331) with Karlsson's data is shown in Fig. 7. The predicted values are in excellent agreement. For the unsteady calculations comparisons were made with the data at this same location.

Unsteady Calculations

The procedure for obtaining unsteady flows is similar to the steady solution procedure. Whereas in the steady state case, the inflow and outer edge boundary conditions are perscribed to be invariant in time, for the unsteady case the velocities at these boundaries are allowed to change in time. For the outer boundary this poses no difficulty since the streamwise velocity is known, i.e.

$$u = u_0(1 + A\cos\omega t)$$

However, there is some difficulty at the upstream boundary where the streamwise velocity is unknown. Several methods have been used by investigators (Ref. 33 - 36) to handle the specification of these upstream conditions. In references 34 and 35, the authors begin their calculation at x_1 = 0 as a

laminar flow and arbitrarily specify a location for instantaneous transition, to fully turbulent flow. Although such a procedure can be employed when the governing equaions are cast in boundary layer coordinates (e.g., $\eta=y/\sqrt{2x}$) in order to remove the singularity at $x_1 = 0$, it necessitates the consideration of transition which we have attempted to avoid. Others, (Ref. 33 and 36) have specified quasi-steady upstream conditions, in which c_f and δ are varied (the parameters in the Cole's velocity profile) to correspond to a steady state that would exist with the same edge velocity at that instant in time. This method also has drawbacks, since the upstream profile is void of any phase shift effects, and this is incompatible with the rest of the flow downstream of that location.

In the present procedure the upstream profile is still given by the Cole's wall-wake velocity profile, but now C_f and δ^* are allowed to be periodic functions of time; i.e.,

$$C_f = C_{f_0}(1 + AC_{f_1} \cos(\omega t + \phi_{C_f}))$$
$$\delta^* = \delta^*_0(1 + A\delta^*_1 \cos(\omega t + \pi + \phi_{\delta^*})) \qquad (44)$$

where c_{f_0} and δ^*_0 are the mean (time averaged) skin function and displacement thickness, c_{f_1} and δ^*_1 are their respective amplitudes of oscillation and ϕ_{c_f} and ϕ_{δ^*} their respect phase shifts. This procedure introduces additional unknowns. For the mean quantities c_{f_0} and δ^*_0, the steady state values are used, while the other four quantities are determined by analyzing the solution behavior near the upstream boundary. For instance the variation of ϕ_{c_f} as a function of the reduced frequency $\omega x/u_o$ is shown in Fig. 8. As can be seen, the quasi-steady upstream profile is not consistent with the interior, while the present procedure gives more realistic behavior leading to a smoother transition from the upstream to the interior. Although $\omega x/u_o$ may not be the unique scaling parameter for turbulent flow, it is nevertheless used in the present approximate analysis which is now briefly described. First, the parameters in Eq. (44) were assumed for the low frequency case, ω = .33 Hz, and a solution was computed. Thereafter, the distributions of c_{f_1}, ϕ_{c_f}, δ^*_1, and ϕ_{δ^*} were obtained as a function of $\omega x/u_o$ in the initial calculation. For another frequency, ω_2 for example, the corresponding values of c_{f_1}, ϕ_{c_f}, δ^*_1 and ϕ_{δ^*} can be determined at the new value of $\omega_2 x^*/u_o$, from a curve such as shown in Fig. 8, where x^* is the location of the upstream boundary.

For all the reported computations a time step corresponding to 10° of the period was chosen. The calculation was run through 2 periods (72 time steps) and the results were obtained for the second period. Several calculations were run through 3 periods and the solutions did not vary from the second period results. Also, several calculations were run in 5° time step increments and again the results were almost indistinguishable from those obtained with 10° time steps, thus indicating accurate temporal resolution. The run time for a 36 x 51 grid is 44.91 sec on the CRAY-1 for three cycles (108 time steps) and corresponds to .00024 sec/grid point/time step.

In presenting the results, the skin friction, C_f, the displacement thickness, δ^* and the streamwise velocity profile at the measuring station were Fourier decomposed into their harmonic components.

For a function $f(\tau)$, the Fourier Series becomes:

$$f(\tau) = \frac{a_0}{2} + \sum_{n=1}^{\infty} \left\{ a_n \cos \omega n t + b_n \sin \omega n t \right\}$$

where

$$a_0 = \frac{\omega}{\pi} \int_{t_1}^{t_1 + T} f(\xi) d\xi$$

$$a_n = \frac{\omega}{\pi} \int_{t_1}^{t_1 + T} f(\xi) \cos \omega n \xi \, d\xi \qquad (45)$$

$$b_n = \frac{\omega}{\pi} \int_{t_1}^{t_1 + T} f(\xi) \sin \omega n \xi \, d\xi$$

and where t_1 is the time at the start of the integration, and the period $T = 2\pi/\omega$.

Although the code allows for the determination of any number of harmonics, only the first two were obtained. In Karlsson's experiment, the mean (time averaged) velocity and the components of the first harmonic were measured. Therefore, comparing to the Fourier series representation the mean velocity is $a_0/2$, the in phase component of the first harmonic is a_1 and the out of phase component of the first harmonic is $-b_1$ (to correspond to Karlsson's notation). For the evaluation of the Fourier coefficients Simpson's integration scheme was used and all data points for the second cycle were sampled.

Results of the computations and comparisons with the data of Karlsson are shown in Figs. 9-22. In the first set, Figs. 9-13, the time averaged

mean velocity profiles of the location corresponding to Karlsson's streamwise measuring station are shown for frequencies ω = .33, 1.0, 1.33, 2.0, 4.0 and 7.7 Hz with amplitudes of oscillation A = .2020, .195, .1763, .1358 and .1273 respectively. As can be seen in these figures, there is excellent agreement between the computed profiles and the data. Since there is little difference between the mean velocity profiles and the quasi-steady profiles, unsteady effects cannot be inferred from an inspection of these figures. Therefore, the in phase and out of phase components of the first harmonic of the oscillations must be considered; corresponding to normalized values of a_1 and $-b_1$ in Eq. 45. These are given in the next set, Figs. 14-18.

As can be seen in these figures, there are considerable unsteady effects present with the predominant effects appearing at the lower frequencies. At the highest frequency calculated, 7.7 Hz, the unsteady effects are relegated to a thin region near the wall reminiscent of the shear wave solutions of Lighthill (Ref. 37) for laminar flows. Note that the boundary layer does not oscillate as a unit at the excited frequency but rather different portions oscillate at varied frequencies. This is further exemplified by the characteristic overshoots and undershoots in the in phase and out of phase components respectively that were obtained for all cases run. For ω = .33 Hz there is excellent quantitative agreement with data for both components, while for the other frequencies considered the correct qualitative behavior was obtained but the exact magnitudes and locations of the peaks were not recovered. It should be noted that the present results show quite good agreement with Karlsson's data even though a simple turbulence model was used. In particular, the characteristic in phase and out of phase velocity profiles were qualitatively predicted and quantitatively these profiles were in agreement with the data. The existing descrepancies, however, could be due to turbulence modeling, upstream conditions or experimental error. It should also be noted that the present in phase and out of phase prediction show better agreement with Karlsson's data than was obtained by other researchers using a variety of turbulence models (e.g. Refs. 42 and 43).

The next two figures 19 and 20 show the amplitude and phase angle variations of the displacement thickness plotted against the reduced frequency $\omega x/u_o$. Also shown in these figures are the data of Karlsson (interpreted by Telionis with his error estimates indicated by vertical bars)

as well as the present predictions for ω = .33, 1.0, 2.0, 4.0 and 7.7 Hz. Good agreement is obtained between the present results and the data as far as amplitude is concerned. In addition, these results compare favorably with those obtained by McCroskey (Ref. 33).

However, the phase angle of the skin friction (phase lead) as a function of reduced frequency (cf. Fig. 21) shows an apparent lack of agreement between the present predictions and the data. Such a discrepancy was also noted in the results of other analyses as shown previously in Fig. 4. A better understanding of these results can be obtained by viewing Fig. 21 which presents the calcuated ϕ_{cf} versus $\omega x/u_o$ for each of the five runs made under the present effort. Each curve represents the results for a different oscillation frequency, ω.

As can be seen in Fig. 21 for each of the frequencies the phase angle approaches a different constant asymptotic value that is increasing with frequency. Each case taken alone resembles the behavior obtained for laminar flow. Whereas in laminar flow the unique similarity variable is the reduced frequency, $\omega x/u_o$, for turbulent flow it may not be. Furthermore, the phase angle is likely to be a function of the Reynolds number as well. Therefore, when viewed in this manner, the present predictions would have the appropriate physical behavior since they mimic the results obtained for laminar flow. Nevertheless, the lack of correlation with the data and the correspondence of the various calculations still needs to be addressed.

The experimental data as well as the other computations in Fig. 4 tend to lie on curves that are monitonically increasing with reduced frequency. Recall that the experimental data correspond to different frequencies at <u>one</u> streamwise location, and not to the phase angle distribution along the plate at a given frequency. If one would connect the points associated with the measuring station for each of the present calculations one would obtain a curve resembling for instance that of McCroskey (Ref. 33) (cf. Fig. 4). The curves obtained by other investigators appear to be based on data points for different values of ω and may not indicate the appropriate physical behavior, nor for that matter they may not contradict the present results. Finally, with regard to the displacement of the various curves, the discrepancy may reside in the virtual origin associated with turbulent flows. Since the streamwise distance is not a characteristic length, the distances in various predictions would not correspond precisely with those of

Karlsson. By taking this into account, and shifting the present data points so that for the ω = .33 Hz case the reduced frequency of the computation is set equal to that of the experimental data the new curve (stars) in Fig. 22 is obtained.

Three-Dimensional Calculation

The three-dimensional unsteady flow requires additional attention compared to its two-dimensional counterpart, ir particular with respect to boundary condition specification. For two-dimensional flows at the upstream inflow boundary (which is a line) the streamwise velocity profile must be specified as a function of time. For the three-dimensional flow, there are two inflow boundaries (planes) (cf. Fig. 2) where streamwise as well as spanwise velocity profiles must be specified. Since the intent of this calculation is to demonstrate the capability of computational procedure for three-dimensional unsteady flows, the boundary conditions at these boundaries were obtained from the two-dimensional results. The description of the actual steps in the calculation are now given.

First, the analogous two-dimensional steady and unsteady calculations were completed. The normal and streamwise velocity profiles were then stored for each time step during the second cycle of the oscillating flow. This corresponds to the flow along the diagonal of the square computational domain. For the two-dimensional problem the extent of the computational domain was .960 m $\leq x_1 \leq$ 4.526 m (3.15 ft $\leq x_1 \leq$ 14.85 ft) and $0 \leq x_3 \leq$ .122 m ($0 \leq x_3 \leq$ .4 ft) and a 27 by 41 grid was employed. In the streamwise direction, a uniform grid was employed with Δx_1 = .137 m (.45 ft) while normal to the wall a hyperbolic transformation was used to cluster points near the wall. The setting of the upstream profile was discussed previously. In anticipation of the three-dimensional problem to be done the upstream x_1 location was located at x_1 = .960 m (3.15 ft) rather than .594 m (1.95 ft). Therefore, the Cole's velocity profile required different values of $Re_{\delta*}$ and c_f which were set to 1200 and .0043, respectively. Steady state was reached in 38 time steps with a total running time of 9.545 seconds or .00023 sec/grid point/time step. Thereafter the unsteady case was run for ω = .33Hz and with an amplitude of oscillation, A = .202. The modified upstream condition procedure was used, with the following parameters set

$$\delta^*_1 = .28 \qquad c_{f_1} = 1.82$$

$$\phi_{\delta^*} = 24^\circ \qquad \phi_{cf} = 4^\circ$$

The calculation was run for two periods with a time step corresponding to 10° and the Fourier decomposition was computed on the second cycle. Results of the calculation are shown in Figs. 9 and 14. The mean flow and the in-phase and out-of-phase components are in excellent agreement with the data. The phase shifts angles and amplitudes show qualitatively the same behavior as the calculations of McCroskey and Phillipe (Ref. 33).

Having obtained the two-dimensional unsteady results, a three-dimensional flow field calculation can be made. The first task is to determine a starting flow field for the three-dimensional calculation. Since a periodic solution is sought, the flow field at the beginning of a cycle will not necessarily correspond to the steady state flow field, but rather to the cyclical flow. In order to reduce total computational time, the initial flow field used to run the 3-D calculation was that which was obtained at the beginning of the second cycle of the two-dimensional calculation. Recall that the two-dimensional calculation corresponds to the flow along the diagonal of the computational domain in the ξ coordinate direction. Hence, in order to obtain the initial flow field the two-dimensional data was reflected directly onto the grid by decomposing the ξ direction velocity into its x_1 and x_2 components. This was done in order not to interpolate the two-dimensional calculation onto the three-dimensional grid. This resulted in a 14 × 14 grid in the x_1–x_2 plane and a grid spacing of $\Delta x_1 = \Delta x_2 = .194$ m (.636 ft). Since this spacing is larger than that used for the two-dimensional calculation, there is a question to what effect that discretization error would have on the solution. Therefore, another coarser two-dimensional calculation was performed on a 20 × 41 grid which corresponded to the same Δx_1 as the three-dimensional calculation, and the results obtained were very close to the fine mesh calculation.

Once the initial flow field was obtained, the three-dimensional calculation was run, also with a 10° time step, but for only one cycle. Since the initial state is obtained from a periodic solution there is no need to march through one preliminary cycle in order to eliminate transient non-periodic effects. The inflow boundary conditions as stated previously were the two-dimensional unsteady results, decomposed into their x_1 and x_2 components, and applied along boundaries 1 and 2 in Fig. 2.

The results for the mean flow and the in phase and out of phase components of the first harmonic of the velocity were indistingushable from the two-dimensional results (cf. Figs. 9 and 14). This indicates that the three-dimensional procedure can give accurate results comparable to the two-dimensional calculation. However, further validation was obtained by comparing the three-dimensional derived boundary layer properties with the two-dimensional results along a ξ = constant line (perpendicular to the diagonal). Along such a line the values should be equal to the two-dimensional results. In Table 1 these quantities are presented as a function of plane location corresponding to points along the line perpendicular to the diagonal in the adjacent sketch.

In the first column, the two integers signify the x_2 and x_1 grid locations in that order. Also given in the table are the 27 x 41 fine and 20 x 41 coarse, two-dimensional calculations. As can be seen, the values along the diagonal are relatively constant and the maximum relative error betwen the three-dimensional and the fine two-dimensional results are less than 0.6%. The minimal variation of these derived values along the ξ = constant line indicates that the three-dimensional calculation procedure recovered the two-dimensional results, hence, further validating the technique. Since the solution is ostensibly two-dimensional in the appropriate frame of reference, the physical behavior corresponds to that which was discussed previously and thus the reader is referred to that section.

As a final note, the reader is referred to Table 2 where run times (total and per grid point per time step) are given for both two-dimensional and three-dimensional results. These run times are for the unvectorized code. If past experience with vectorizating other fluid mechanics codes holds for this code then one can expect a reduction of up to a factor of five in run time. Hence, it is conceivable that three-dimensional viscous calculations of the type considered in this report can be obtained in less than a minute of CPU time on the CRAY-1 computer.

CONCLUSIONS

In the Phase I effort, all major objecties have been satisfied. The three-dimensional solution procedure for the approximate form of the Navier-Stokes equation was exercised in the two- and three-dimensional modes to compute the unsteady turbulent boundary layer on a flat plate corresponding to the data of Karlsson. New upstream boundary conditions were developed that yielded more realistic solutions for the interior in the vicinity of the upstream boundary. Comparisons of the computaion employing these boundary conditions with the data indicate that both qualitative and quantitative agreement was obtained for the mean velocity and the in phase and out of phase components of the first harmonic of the velocity.

In addition, the calculation gave results for the skin friction phase angle that had plausible physical behavior for large distances downstream of the inflow boundary. Finally, an explanation was suggested to resolve the discrepancy with regard to previously reported calculations of the skin friction phase angle.

For the three-dimensional case, the two-dimensional data of Karlsson was considered, but skewed at 45° by a coordinate rotation. The results of the calculations were in excellent agreement with the data and the two-dimensional computations, thereby validating the three-dimensional procedure.

ACKNOWLEDGEMENT

The authors wish to acknowledge the assistance given by Dr. L. W. Carr in supplying the digitized data for Karlsson's experiment.

REFERENCES

1. Sanford, M.C., Ricketts, R.H., Cazier, F.W. and Cunningham, H.J.: Transonic Unsteady Airloads on an Energy Efficient Transport Wing with Oscillating Control Surfaces, Journal of Aircraft, Vol. 18, No. 7, July 1981.

2. Ricketts, R.H, Sanford, M., Seidel, D.A. and Watson, J.J.: Transonic Pressure Distributions on a Rectangular Supercritical Wing Oscillating in Pitch, NASA TM 84616, March 1983.

3. Edwards, J.W., Bennet, R.M., Whitlow, W. and Seidel, D.A.: Time Marching Transonic Flutter Solutions Including Angle of Attack Effects, Journal of Aircraft, Vol. 20, No. 11, November 1983.

4. Yates, E.C., Wynne, E.C. and Farmer, M.G.: Effect of Angle of Attack on Transonic Flutter of a Supercritical Wing, Journal of Aircraft, Vol. 20, No. 10, October 1983.

5. Liu, N.-S., Shamroth, S.J. and McDonald, H: Numerical Solution of the Navier-Stokes Equations for Compressible Turbulent Two/Three Dimensional Flows in the Terminal Shock Region of an Inlet/Diffuser, AIAA Paper 83-1892, July 1983.

6. Roscoe, D.V., Shamroth, S.J., Gibeling, H.J. and McDonald, H.: Investigation of Transonic Shock Boundary Layer Interactions, Final Contractor's Report ARO DAAG29-80-C-0082, May 1984.

7. Shamroth, S.J.: Calculation of Steady and Oscillating Airfoil Flow Fields via the Navier-Stokes Equations, AIAA Paper No. 84-0525, 1984.

8. Lin, T.C. and Rubin, S.G.: Viscous Flow Over a Cone at Moderate Incidence, Part 2. Supersonic Boundary Layer, Journal Fluid Mechanics, Vol. 59, Part 3, 1973, pp. 593-620.

9. Briley, W.R.: Numerical Method for Predicting Three-Dimensional Steady Viscous Flow in Ducts. Journal Comp. Physics, Vol. 14, No. 1, 1974.

10. McDonald, H. and Briley, W.R.: Three-Dimensional Supersonic Flow of a Viscous or Inviscid Gas, Journal of Comp. Physics, Vol. 19, No. 2, 1975.

11. Ciment, M., Leventhal, S.H. and Weinberg, B.C.: The Operator Compact Implicit Method for Parabolic Equations, Journal of Comp. Physics, Vol. 23, 1978.

12. Berger, A.E., Solomon, J.M., Ciment, M., Leventhal, S.H. and Weinberg, B.C.: Generalized OCI Schemes for Boundary Layer Problems, Math. Comp., Vol. 35, No. 151, 1980.

13. Briley, W.R. and McDonald, H.: On the Structure and Use of Linearized Block ADI and Related Schemes. Journal of Comp. Physics, Vol. 34, No. 1, 1980.

14. Weinberg, B.C. and McDonald, H.: Solution of Three-Dimensional Time-Dependent Viscous Flows, Part 1: Investigation of Candidate Algorithms. Final Contractor's Report (NAS2-10016), 1979.

15. Weinberg, B.C. and McDonald, H.: Solution of Three-Dimensional Time-Dependent Viscous Flows, Part 2: Development of the Computer Code, Final Contractor's Report, (NAS2-10016), 1980.

16. Howarth, L.: The Boundary Layer in Three-Dimensions - Part I. Derivation of the Equations for Flow Along a General Curved Surface. Philosophical Magazine, Vol. 7, 1951, pp. 239.

17. Roberts, G.O.: Computational Meshes for Boundary Layer Problems. Proceedings of the Second International Conference on Numerical Methods in Fluid Dynamics, Springer-Verlag, New York, 1971, p. 171.

18. Flugge, W.: Tensor Analysis and Continuium Mechanics, Springer-Verlag, 1972.

19. Eiseman, P.R.: The Numerical Solution of the Fluid Dynamical Equations in Curvilinear Coordinates. Air Force Weapons Laboratory Report AFWL-TR-73-172, 1973.

20. Cebeci, T., Kaups, K. and Ramsay, J.A.: A General Method for Calculating Three-Dimensional Comprssible Laminar and Turbulent Boundary Layers on Arbitrary Wings, NASA CR-2777, January 1977.

21. Weinberg, B.C. and McDonald, H.: Solution of Time-Dependent Viscous Flows, Part 3: Application to Turbulent and Unsteady Flows, Final Contractor's Report, (NAS2-10016), 1982.

22. Gibeling, H.J., Shamroth, S.J. and Eiseman, P.R.: Analysis of Strong-Interaction Dynamic Stall for Laminar Flow on Airfoils. NASA CR-2969, April 1978.

23. Favre, A.: Equations des Gaz Turbulents Compressibles. J. de Mecanique, Vol. 4, pp. 361-392, 1965.

24. Kreskovsky, J.P., Shamroth, S.J. and McDonald H.: Application of a General Boundary Layer Analysis to Turbulent Boundary Layers Subjected to Strong Favorable Pressure Gradients, J. of Fluids Engineering, pp. 217-224, June 1975.

25. McDonald, H. and Camarata, F.J.: An Extended Mixing Length Approach for Computing the Turbulent Boundary Layer Development, Proceedings Computation of Turbulent Boundary Layers - 1968 AFOSR-IFP Stanford Conference, Vol. 1, pp. 83-98, 1969.

26. Douglas, J. and Gunn, J.E.: A General Formuation of Alternating Direction Methods. Numerische Math., Vol. 6, 1964, p. 428.

27. Leventhal, S.J.: The Operator Compact Implicit Method for Reservoir Simulation, Proceedings of FIfth SPE Symposium on Numerical Reservoir Simulation, 1979.

28. Blottner, F.G.: Computational Techniques for Boundary Layers in "Computational Methods for Inviscid and Viscous Two and Three-Dimensional Flow Fields". Fluid Dynamics Institute, Hanover, New Hampshire, 1975.

29. Weinberg, B.C., Leventhal, S.H. and Ciment, M.: The Operator Compact Implicit Scheme for Viscous Flow Problems. AIAA Paper No. 77-638. Presented at the 3rd AIAA Comp. Fluid Dynamics Conf., Albuquerque, N.M., 1977.

30. Weinberg, B.C.: Viscous Flow Calcuations Employing a Fourth Order Generalized Operator Compact Implicit Scheme, Paper 79-1468, Presented at 4th AIAA Comp. Fluid Dynamics Conf., Williamsburg, VA, 1979.

31. Karlsson, S.K.F.: "An Unsteady Turbulent Boundary Layer", J.F.M., Vol. 5, 1959, pp. 622-636.

32. Carr, L.W.: "Standardization of Computational Experiments in Unsteady Turbulent Boundary Layer Flow", NASA TM-78445, December 1977.

33. McCroskey, W.J. and Phillipe, J.J.: Unsteady Viscous Flow on Oscillating A°irfoils, AIAA J., Vol. 13, No. 1, Jan. 1975, pp. 71-79.

34. Cebeci, T.: Calculation of Laminar and Turbulent Boundary Layers for Two-Dimensional Time Dependent Flow, NASA CR-2820, July 1977.

35. Murphy, J.D. and Prenter, P.M.: A Hybrid Computing Scheme for Unsteady Turbulent Boundary Layers, Third Symposium Shear Flows, pp. 8.26-8.34, 1981.

36. Singleton, R.E. and Nash, J.F.: A Method for Calculating Unsteady Turbulent Boundary Layers in Two and Three Dimensions, AIAA J., Vol. 12, No. 5, pp. 590-595, 1974.

37. Lighthill, M.J.: The Response of Laminar Skin Friction and Heat Transfer to Fluctuations in the Stream Velocity, Proc. Roy. Soc. 224A, p. 1-23, 1954.

38. Coles, D.E. and Hirst, E.A. (Editors): Proceedings Computation o Turbulent Boundary Layers - 1968. AFOSR-IFP Stanford Conference, Vol. I, Compiled Data, 1969.

39. Clauser, F.H., Boundary Layers in Adverse Pressure Gradients, J. Aeronautical Sci., 21, pp. 91-108, 1954.

40. Musker, A.J.: Explicit Expression for the Smooth Wall Velocity Distribution in a Turbulent Boundary Layer, AIAA J., Vol. 17, 1979, p. 655.

41. Oh, Y.H.: An Analytical Transformation Technique for Generating Uniformly Spaced Computational Mesh. NASA CP-2166, Workshop on Numerical Grid Generation Techniques, 1980, pp. 385-398.

42. Telionis, D.P.: Unsteady Boundary Laeyrs, Separated and Attached, J. Fluids Eng., Vol. 107, pp. 29-43, 1979.

43. Romaniuk, M.S. and Telionis, D.P.: Turbulence Models for Oscillating Boundary Layers, AIAA Paper 79-0069, 1979.

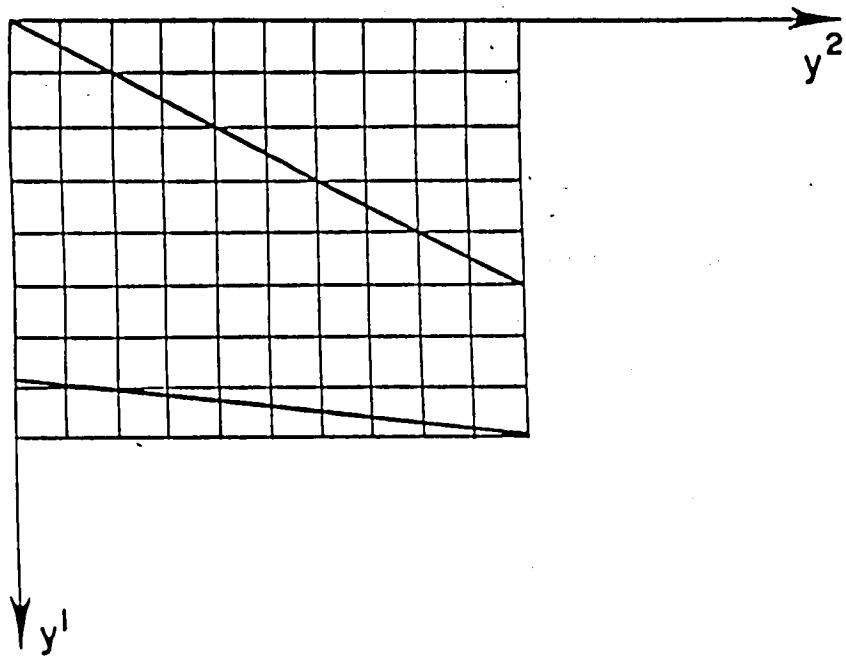

CARTESIAN COORDINATES

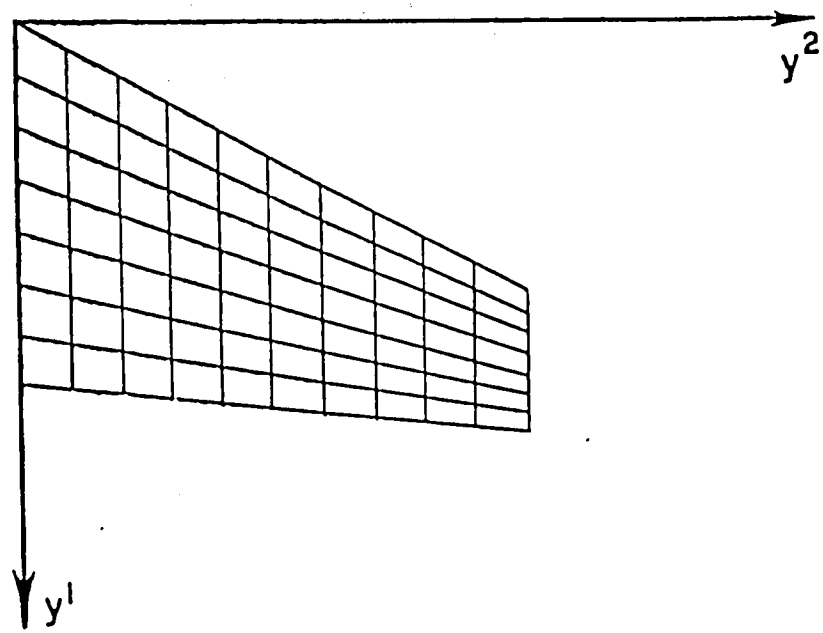

NONORTHOGONAL COORDINATES

Figure 1 - Effect of Coordinate System on Grid Distribution

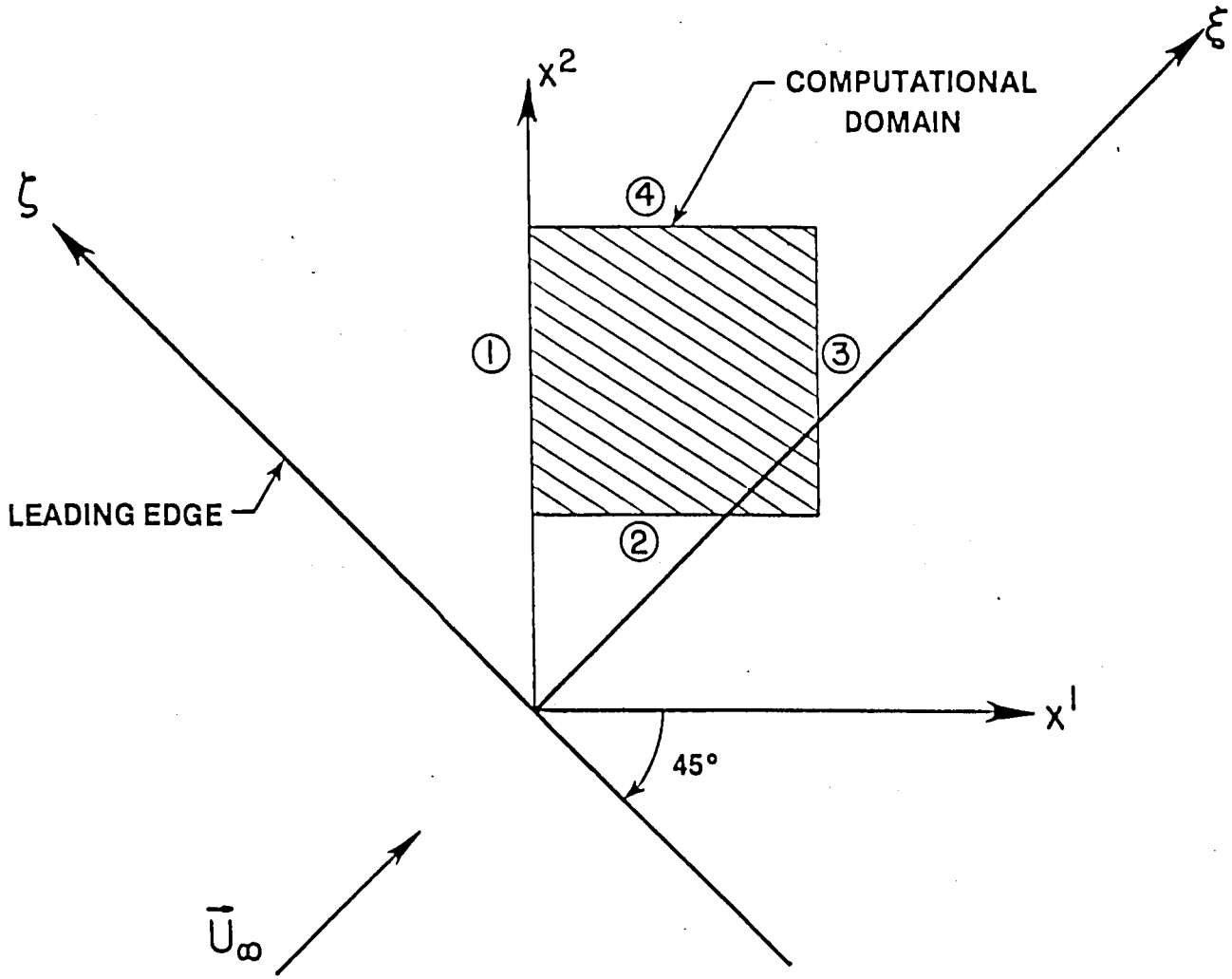

Figure 2 - Three-Dimensional Computational Domain

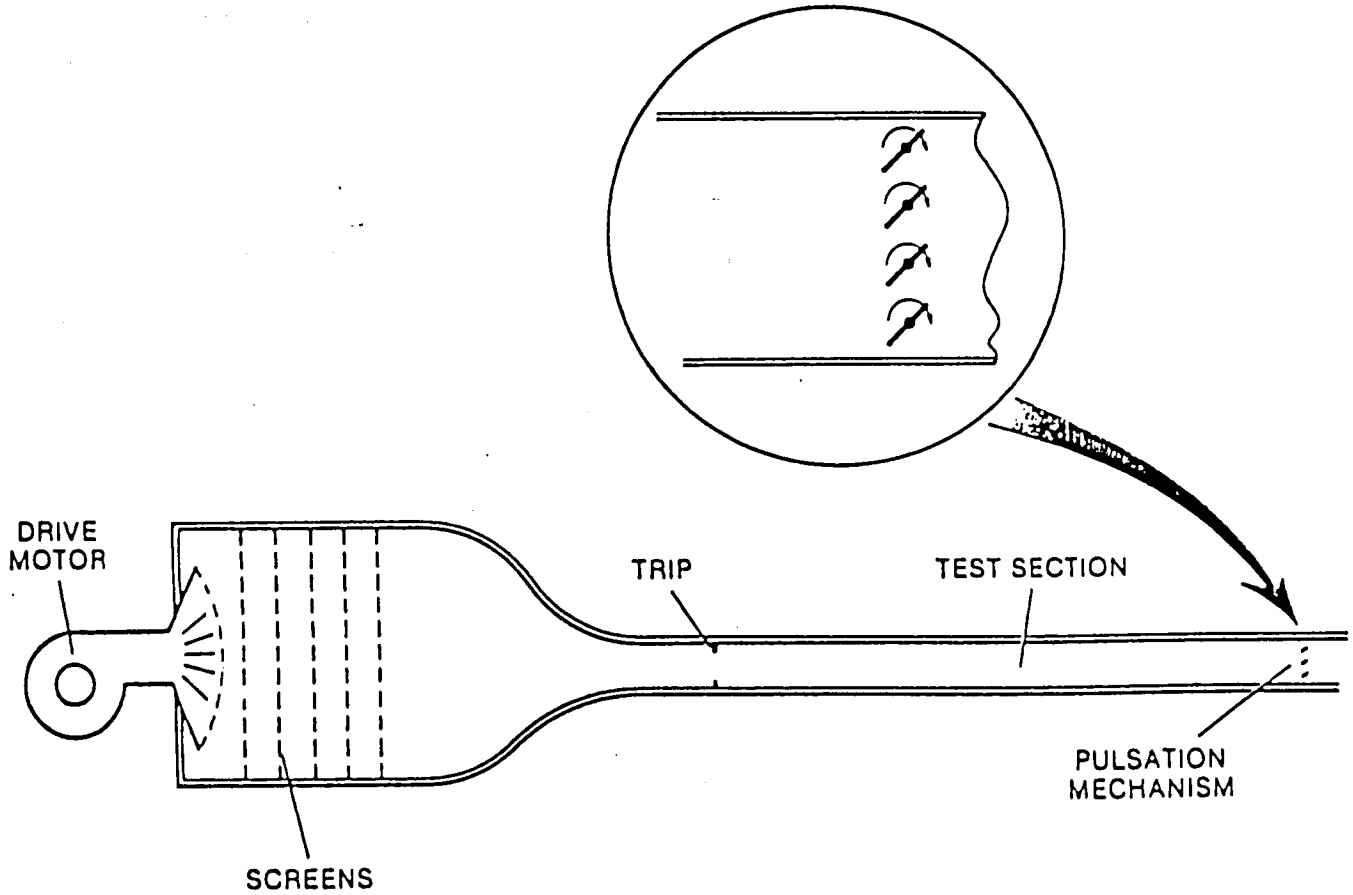

Figure 3 - Schematic of Karlsson's Experimental Facility

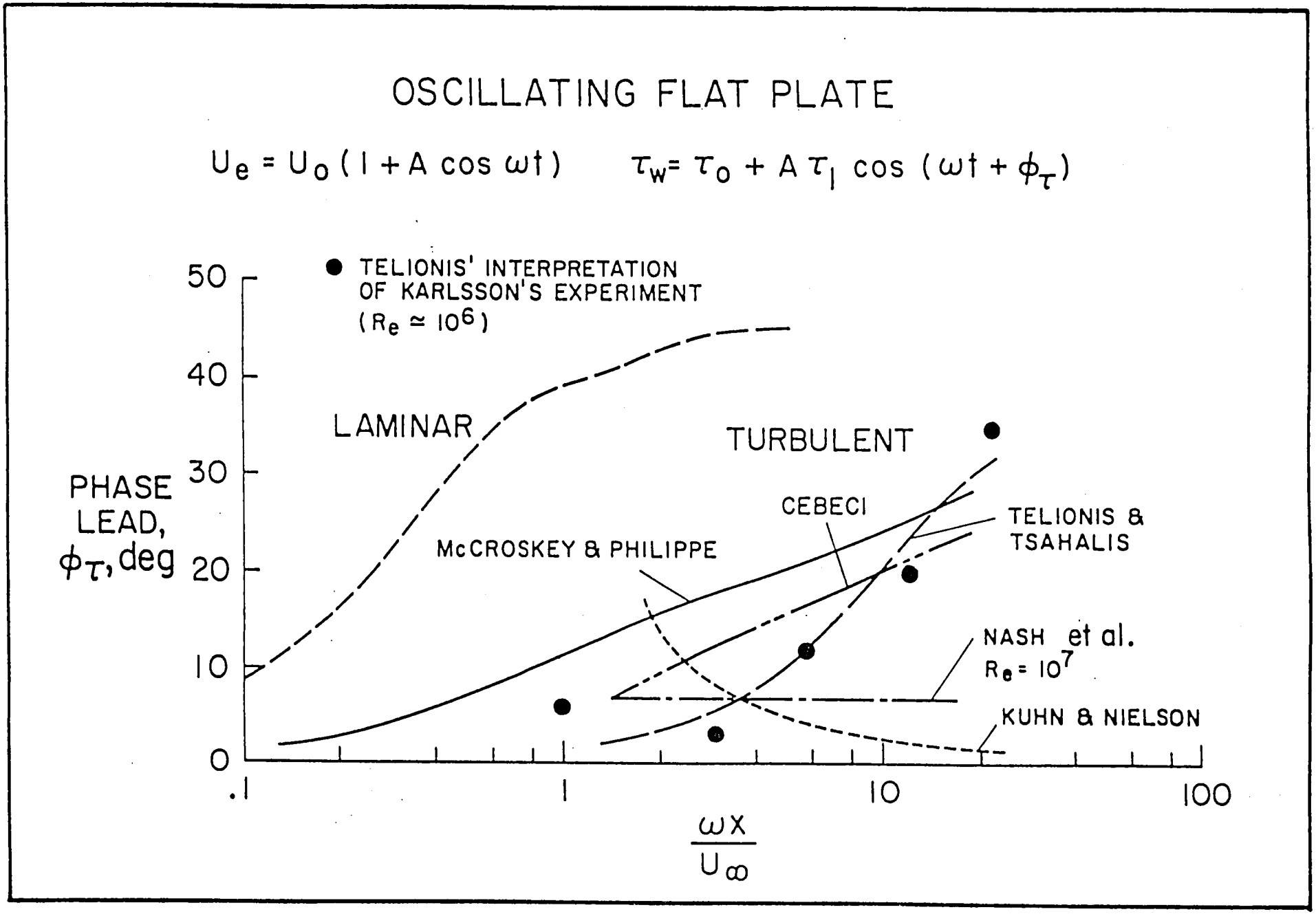

Figure 4 - Phase Lead Angle of Skin Friction as a Function of Reduced Frequency

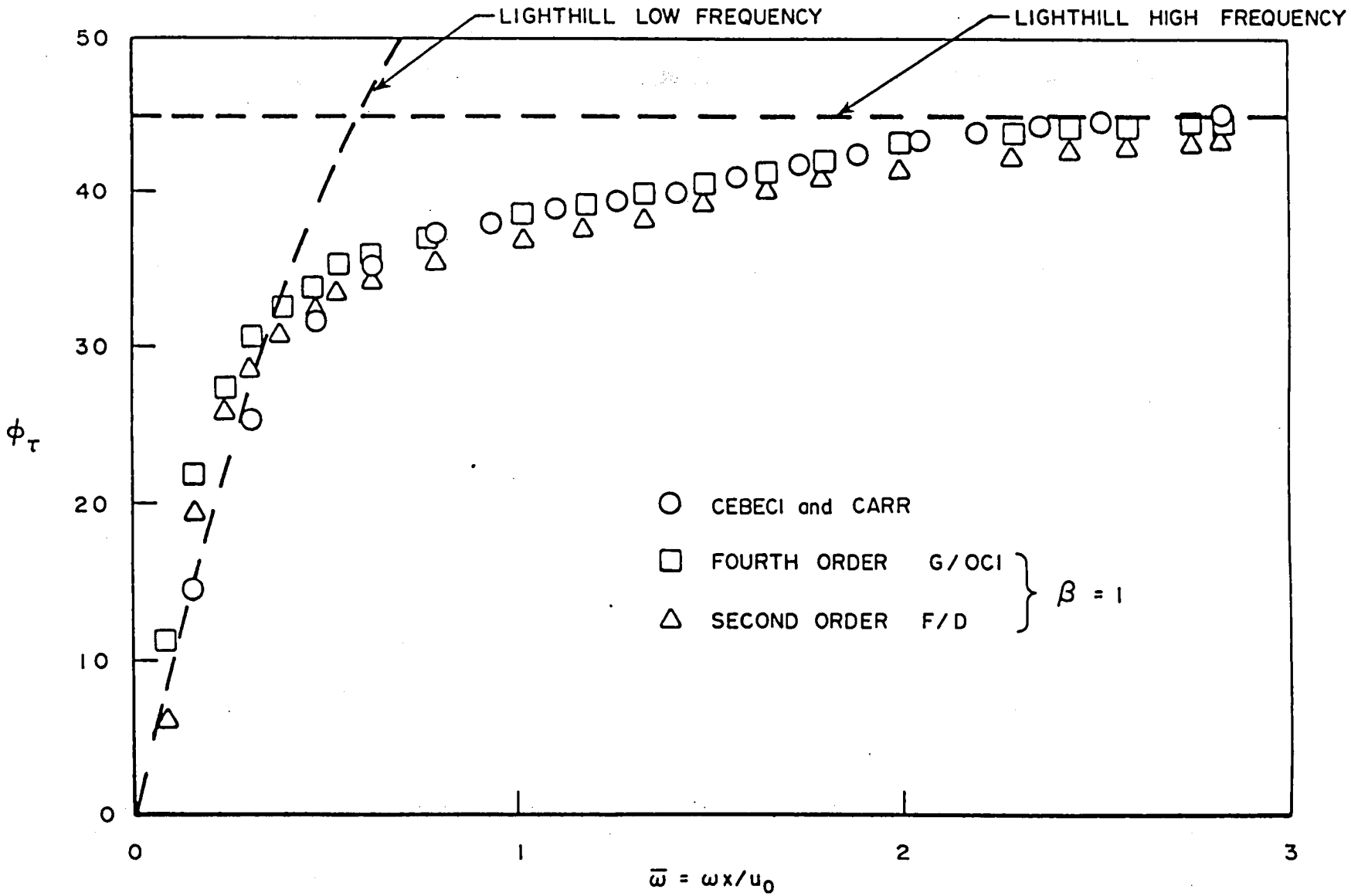

Figure 5 - Phase Angle Between Edge Velocity and Wall Shear Stress for Laminar Flow

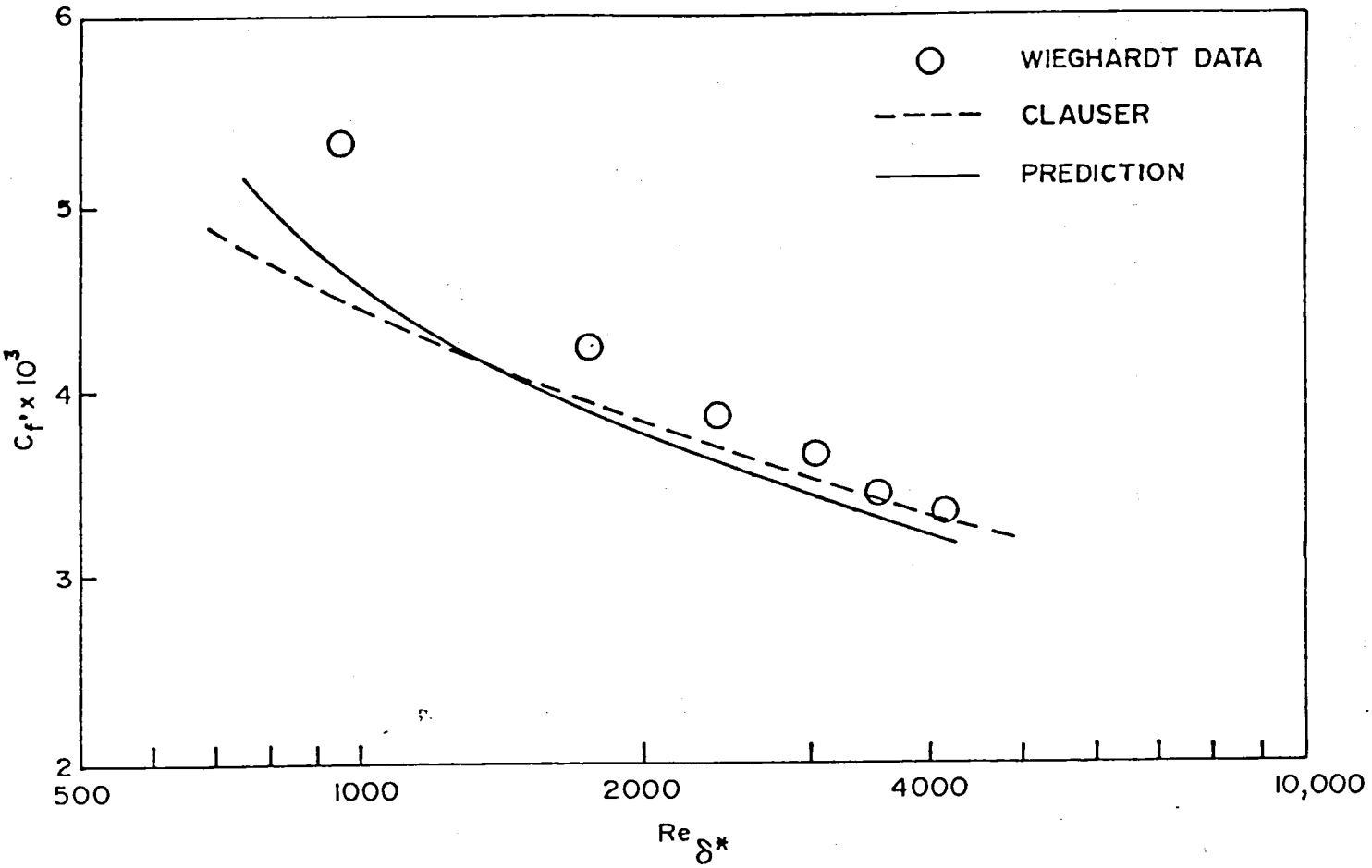

Figure 6 - Skin Friction Coefficient as a Function of Displacement Thickness Reynolds Number

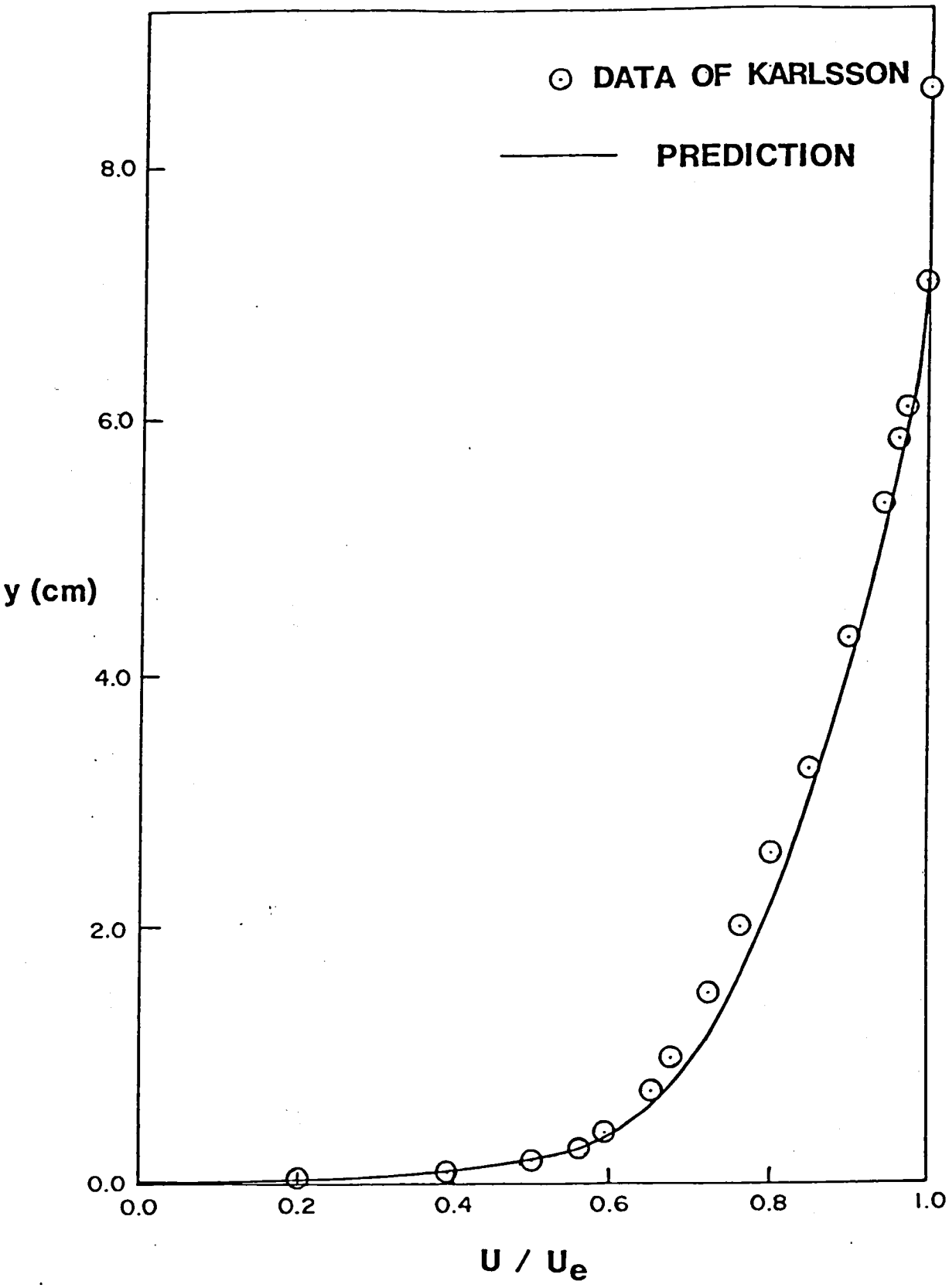

Figure 7 - Quasi-Steady Velocity Profile

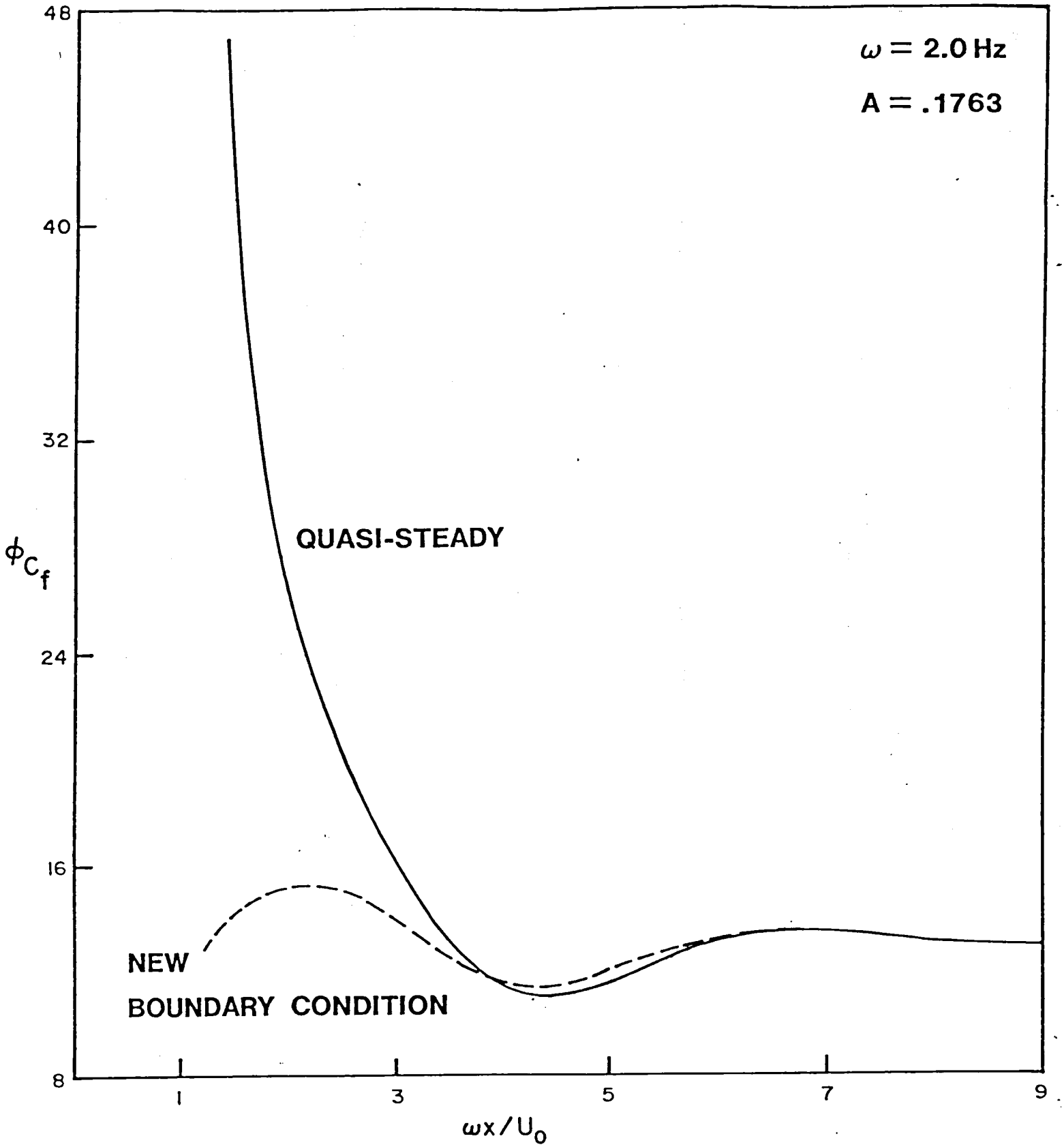

Figure 8 - Effect of Upstream Boundary Condition

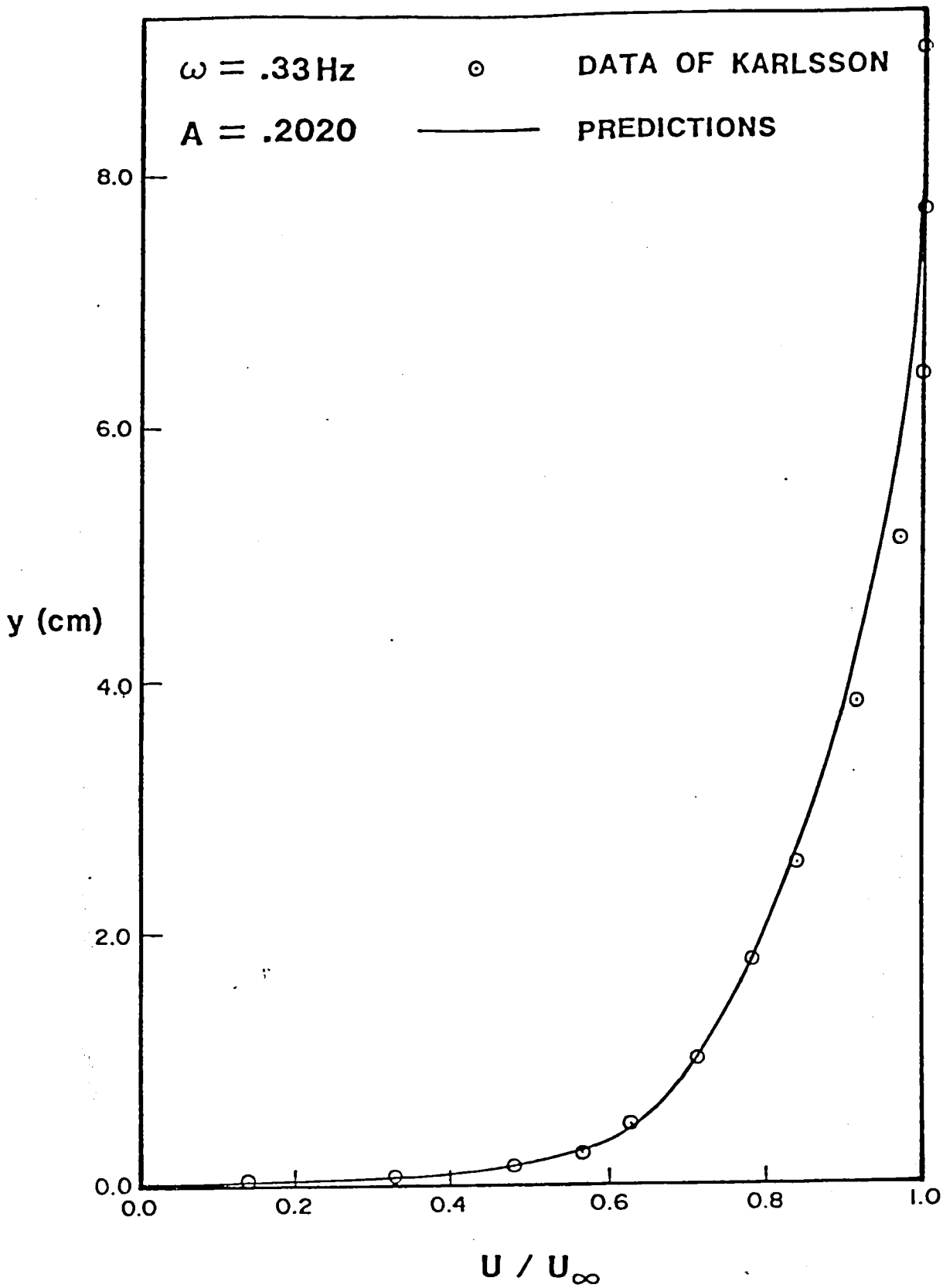

Figure 9 - Mean Velocity Profile

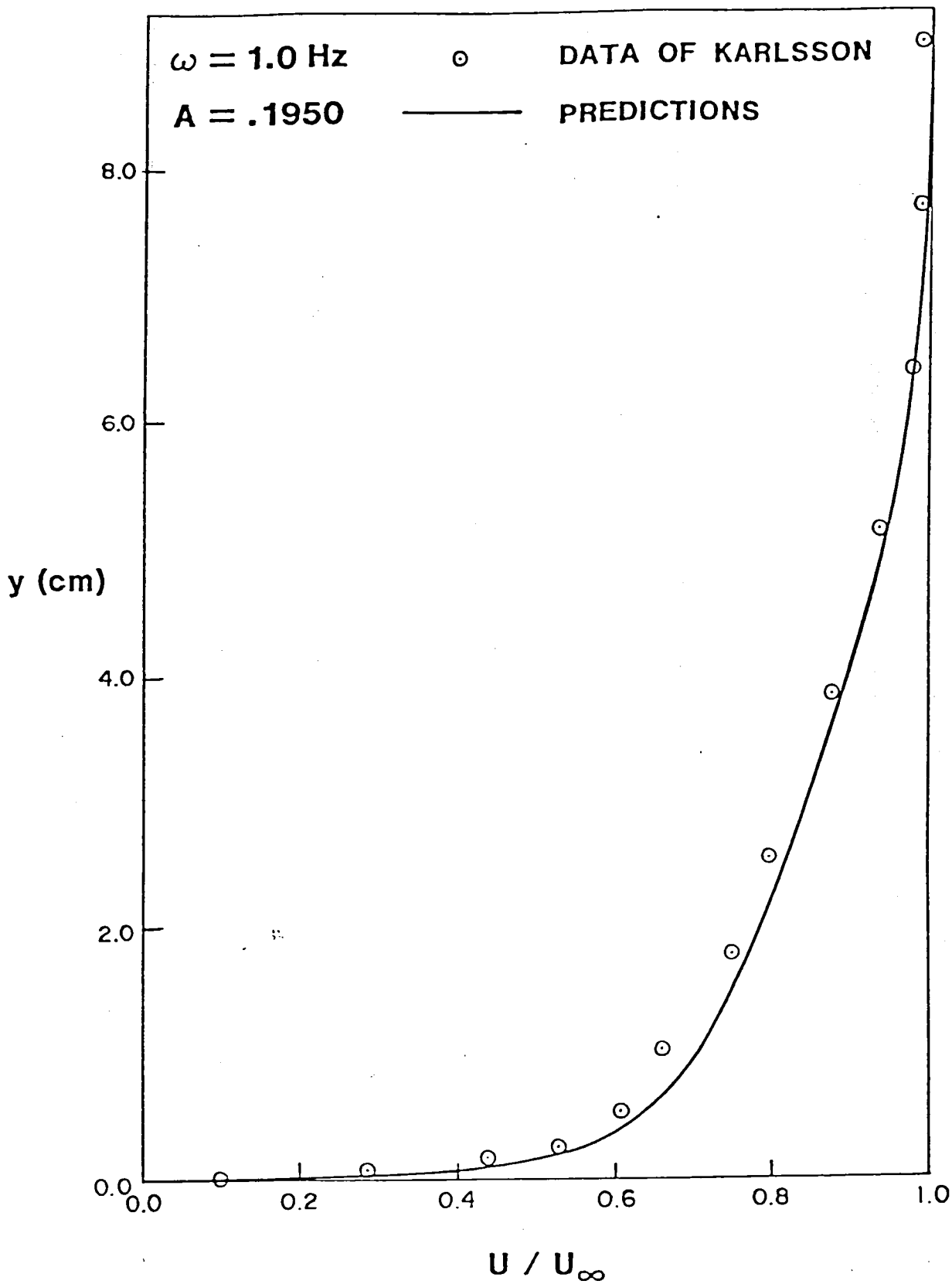

Figure 10 - Mean Velocity Profile

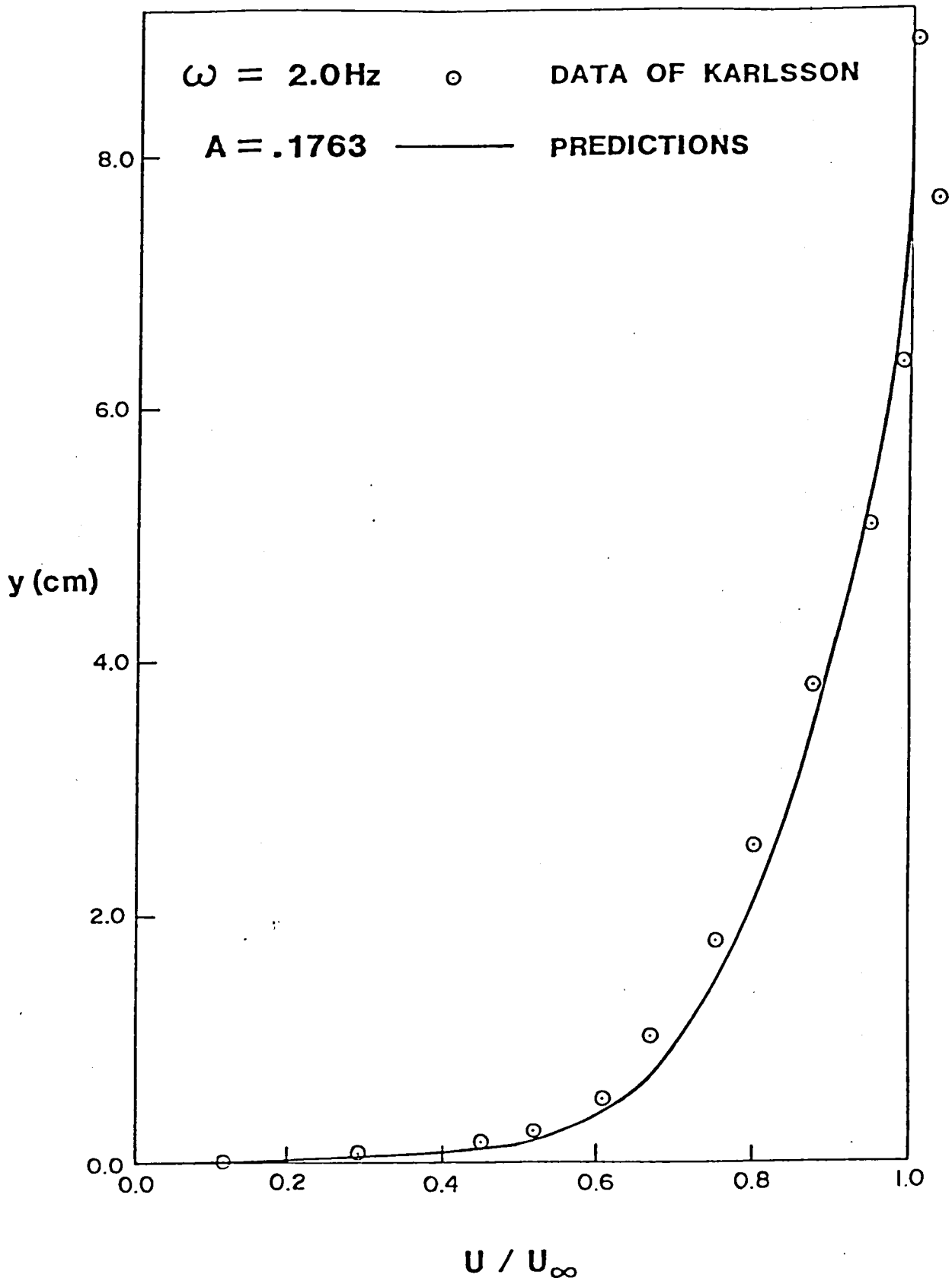

Figure 11 - Mean Velocity Profile

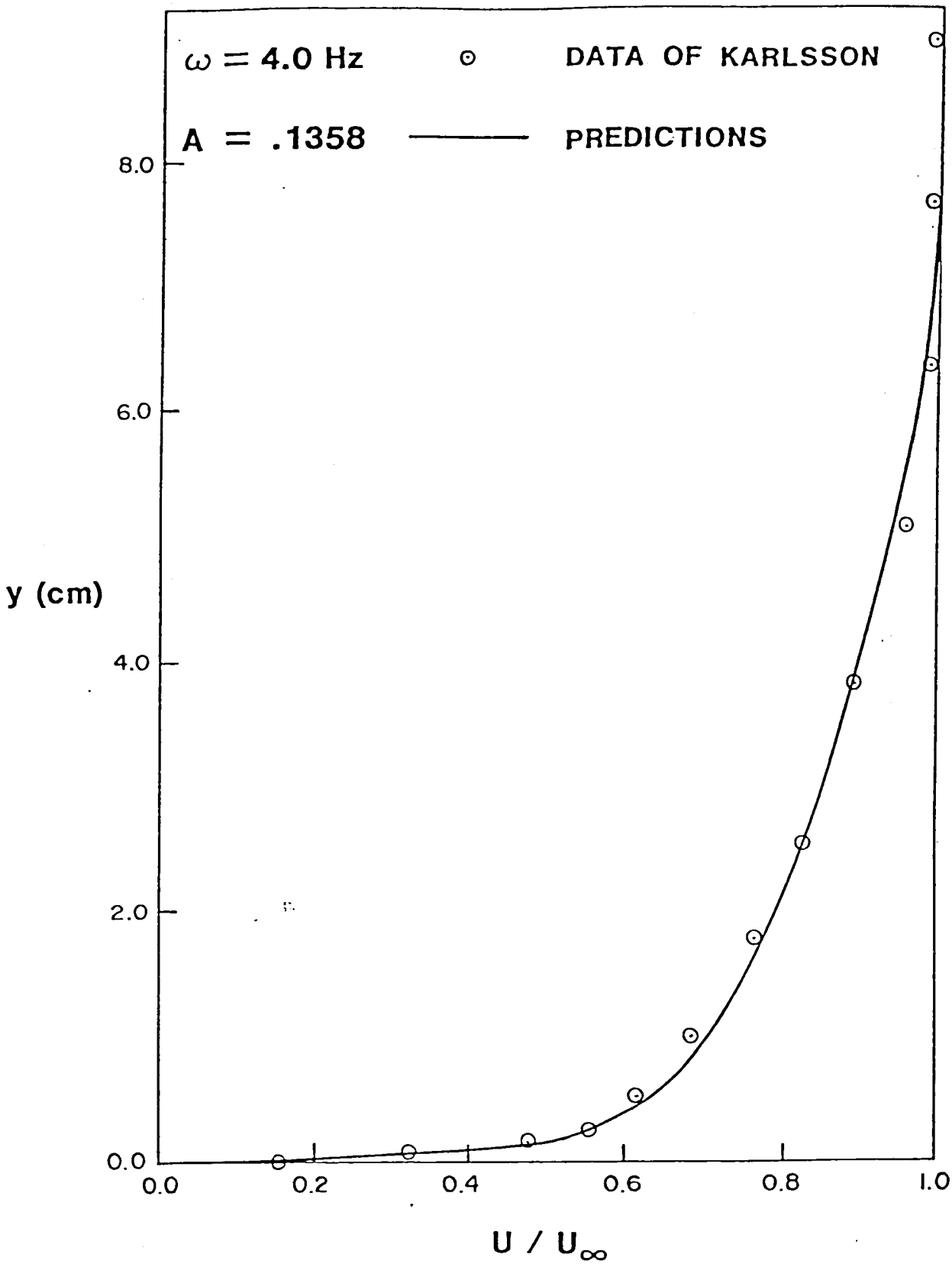

Figure 12 - Mean Velocity Profile

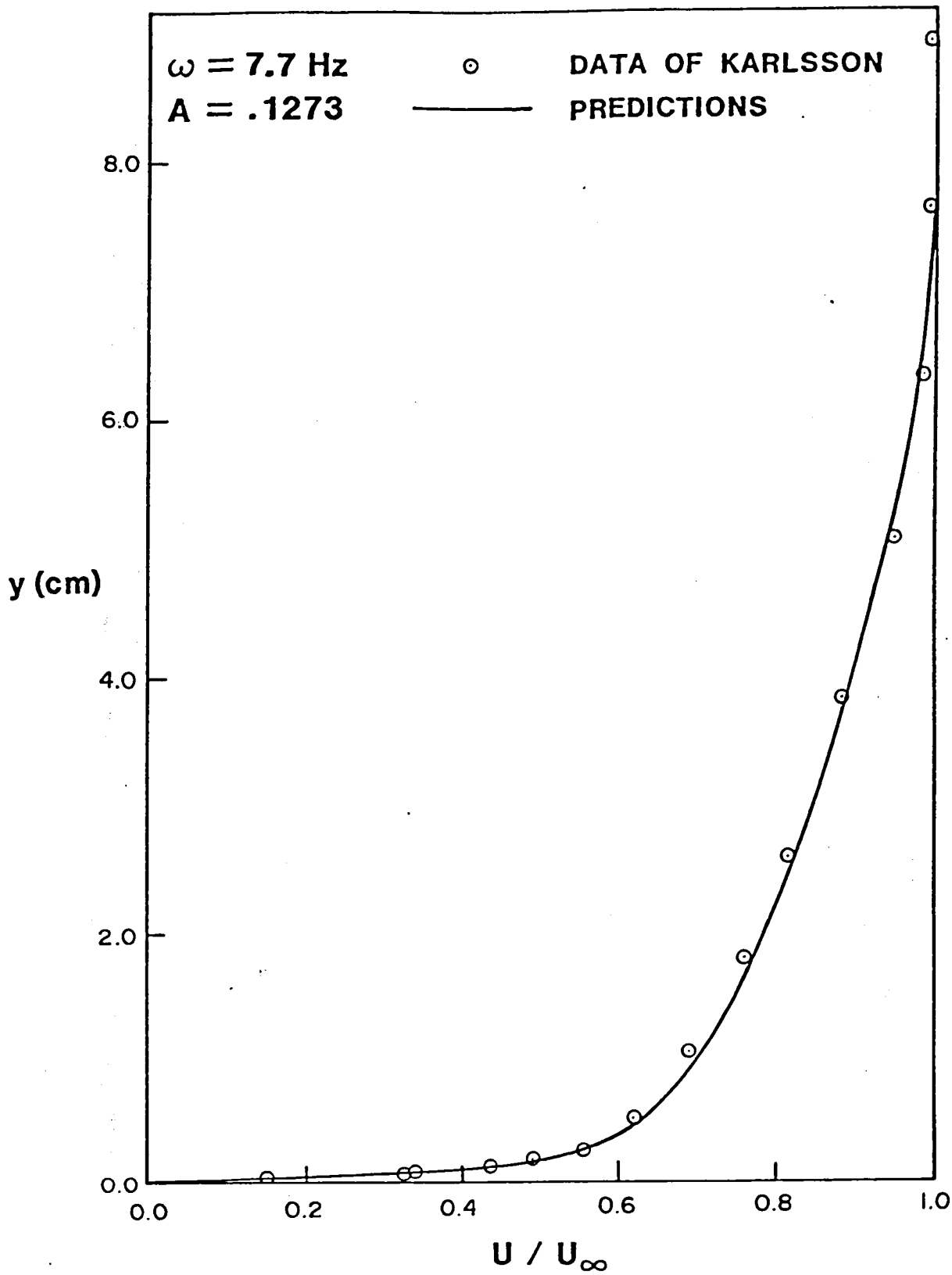

Figure 13 - Mean Velocity Profile

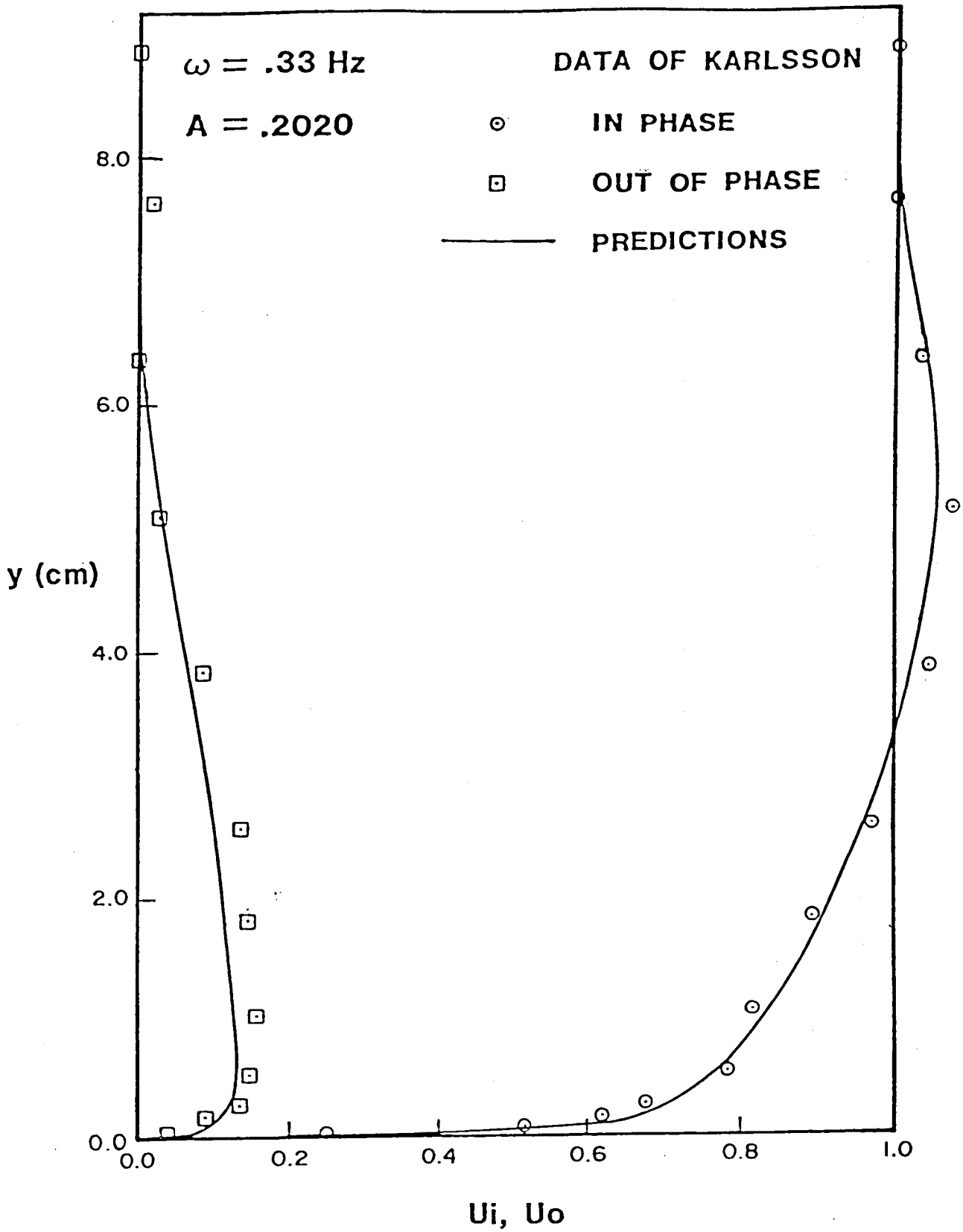

Figure 14 - In Phase and Out of Phase Velocity Components

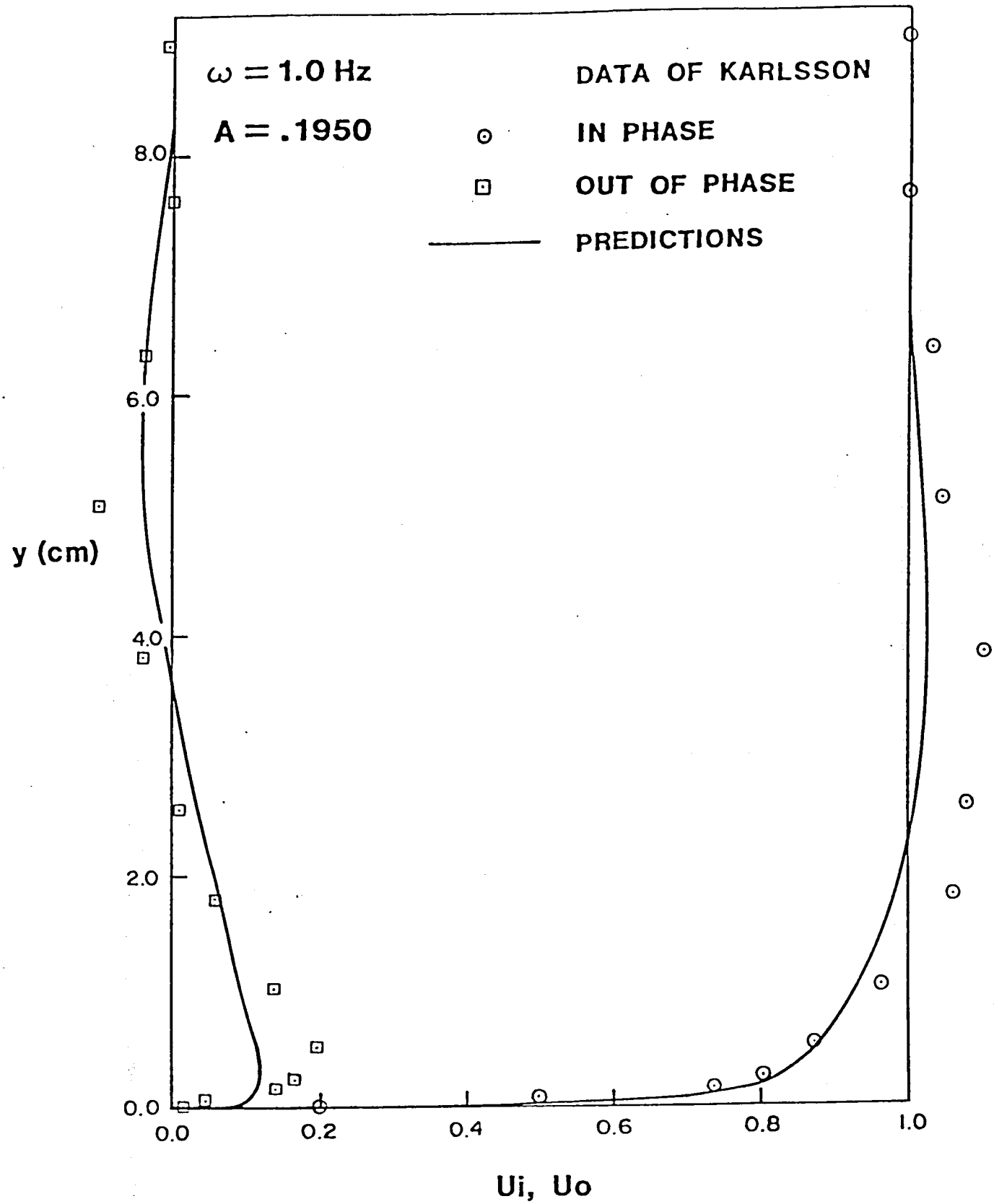

Figure 15 - In Phase and Out of Phase Velocity Components

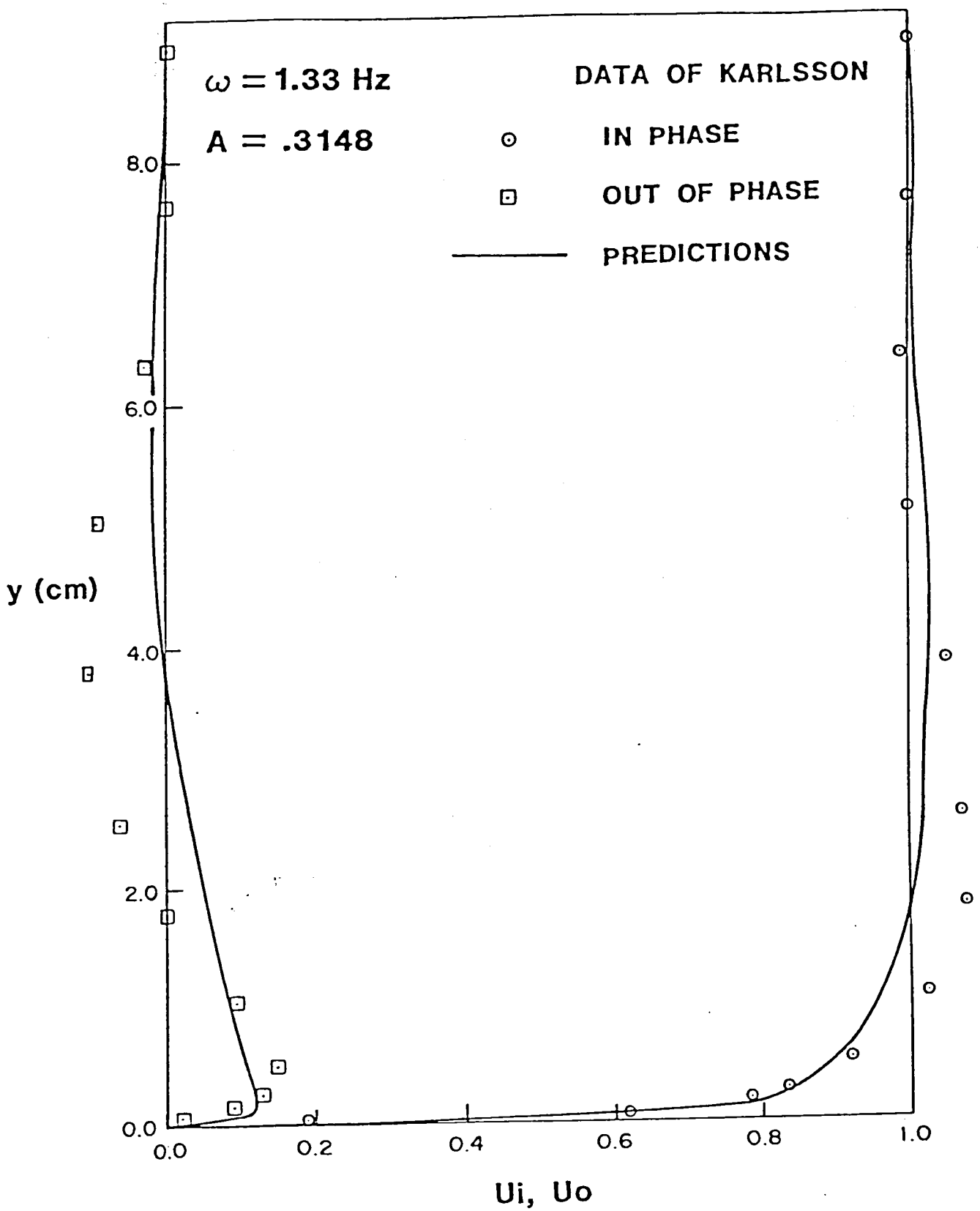

Figure 16 - In Phase and Out of Phase Velocity Components

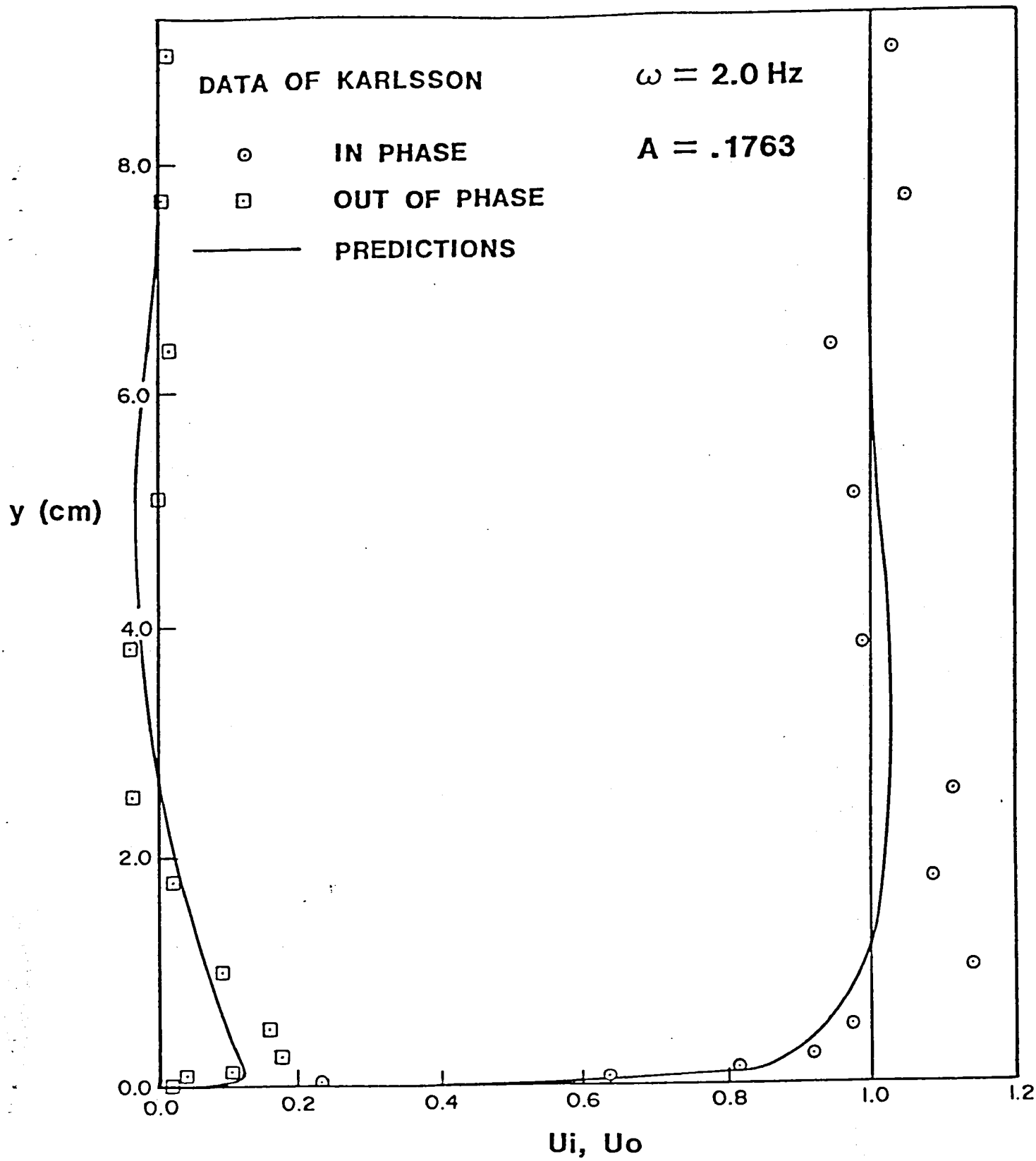

Figure 17 - In Phase and Out of Phase Velocity Components

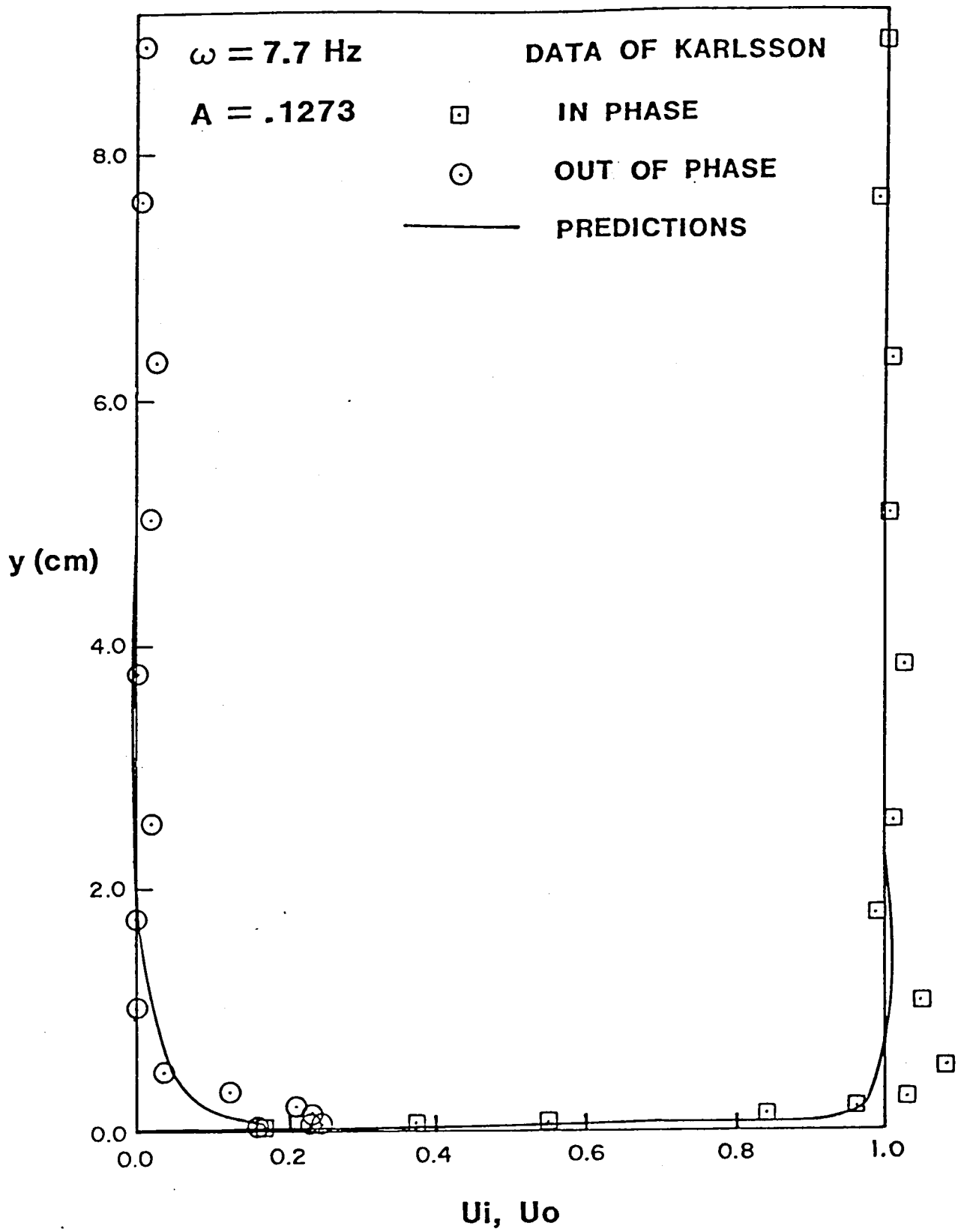

Figure 18 - In Phase and Out of Phase Velocity Components

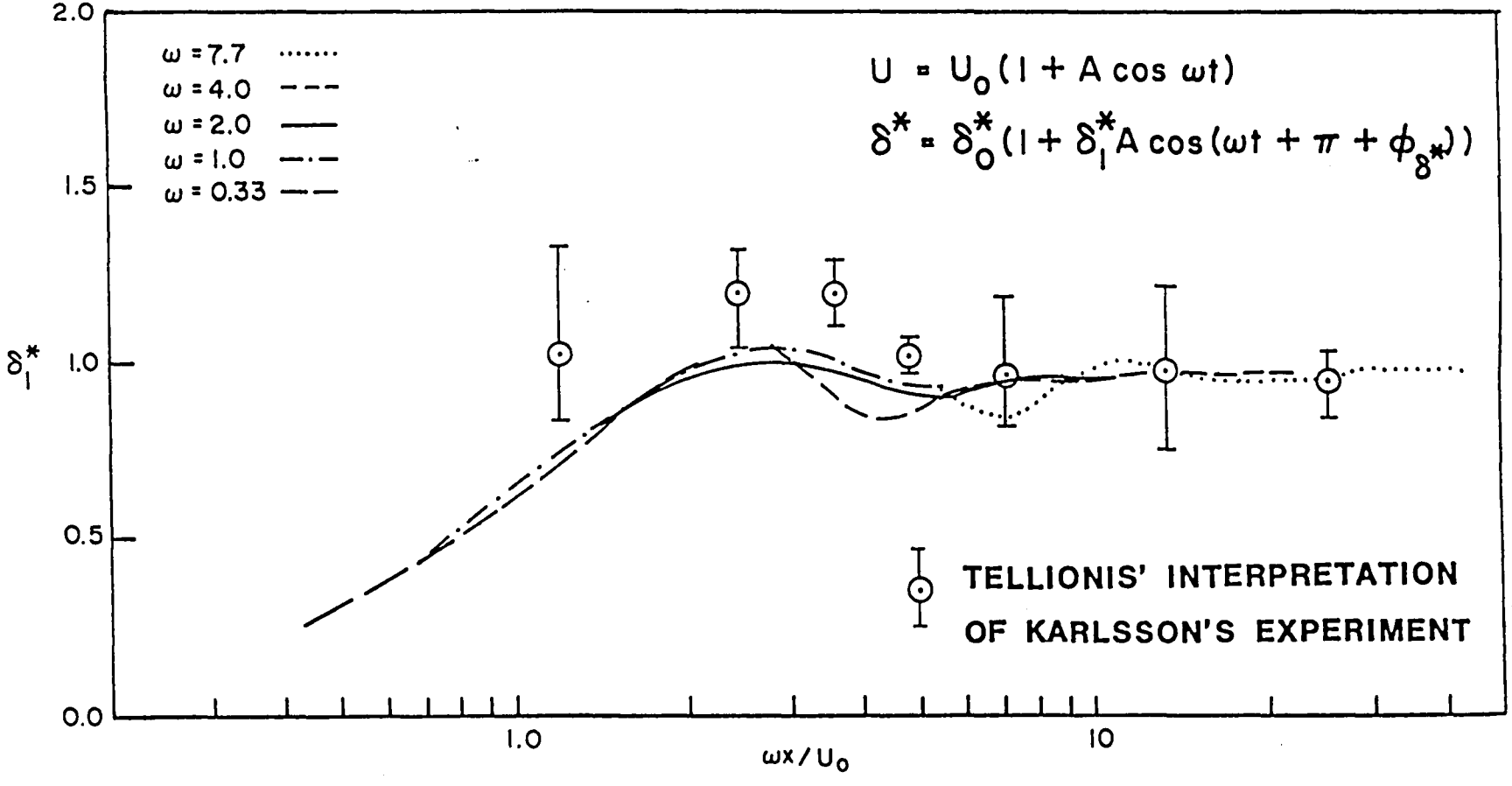

Figure 19 - Amplitude of Displacement Thickness Fluctuations

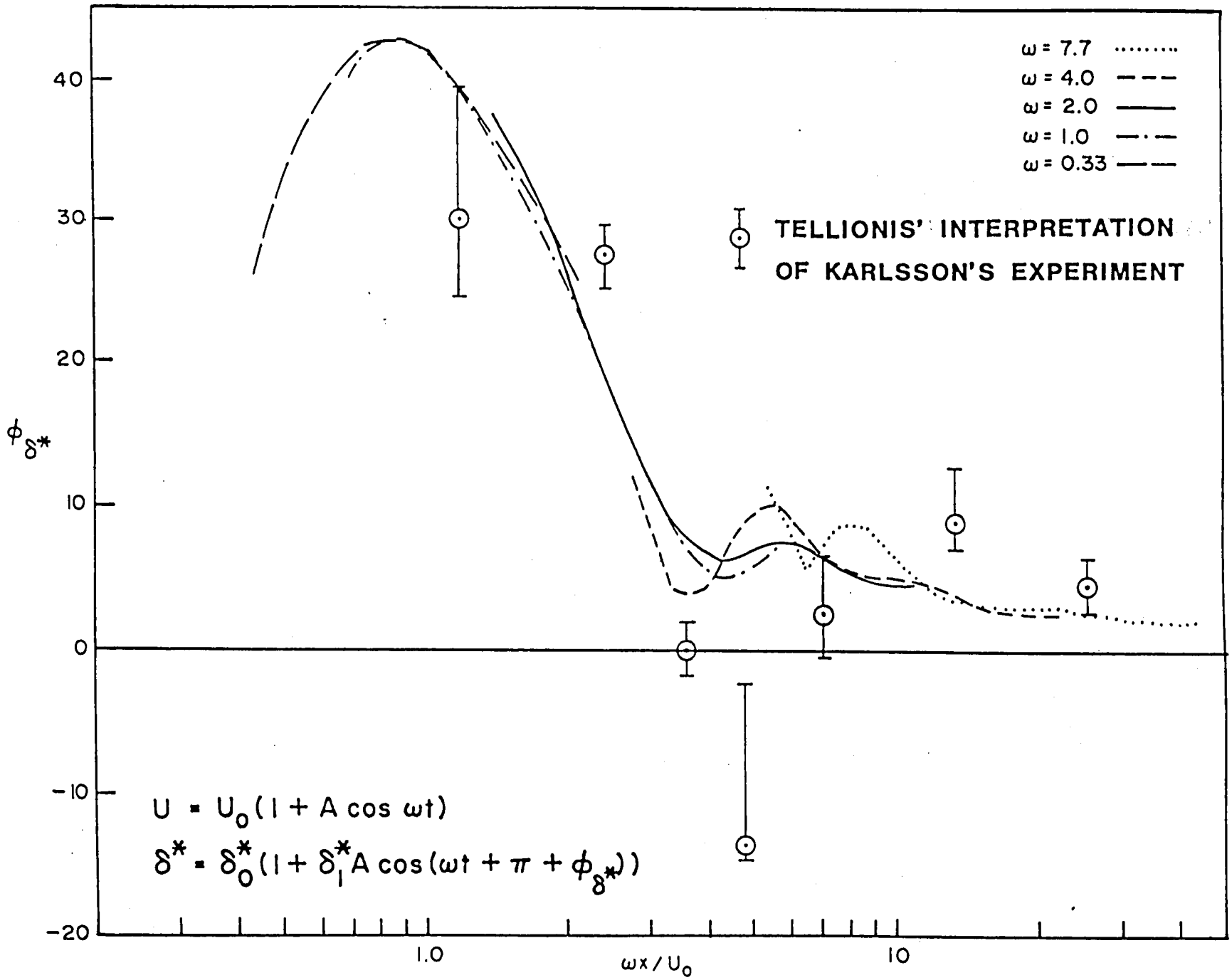

Figure 20 - Phase Angle of Displacement Thickness Fluctuations

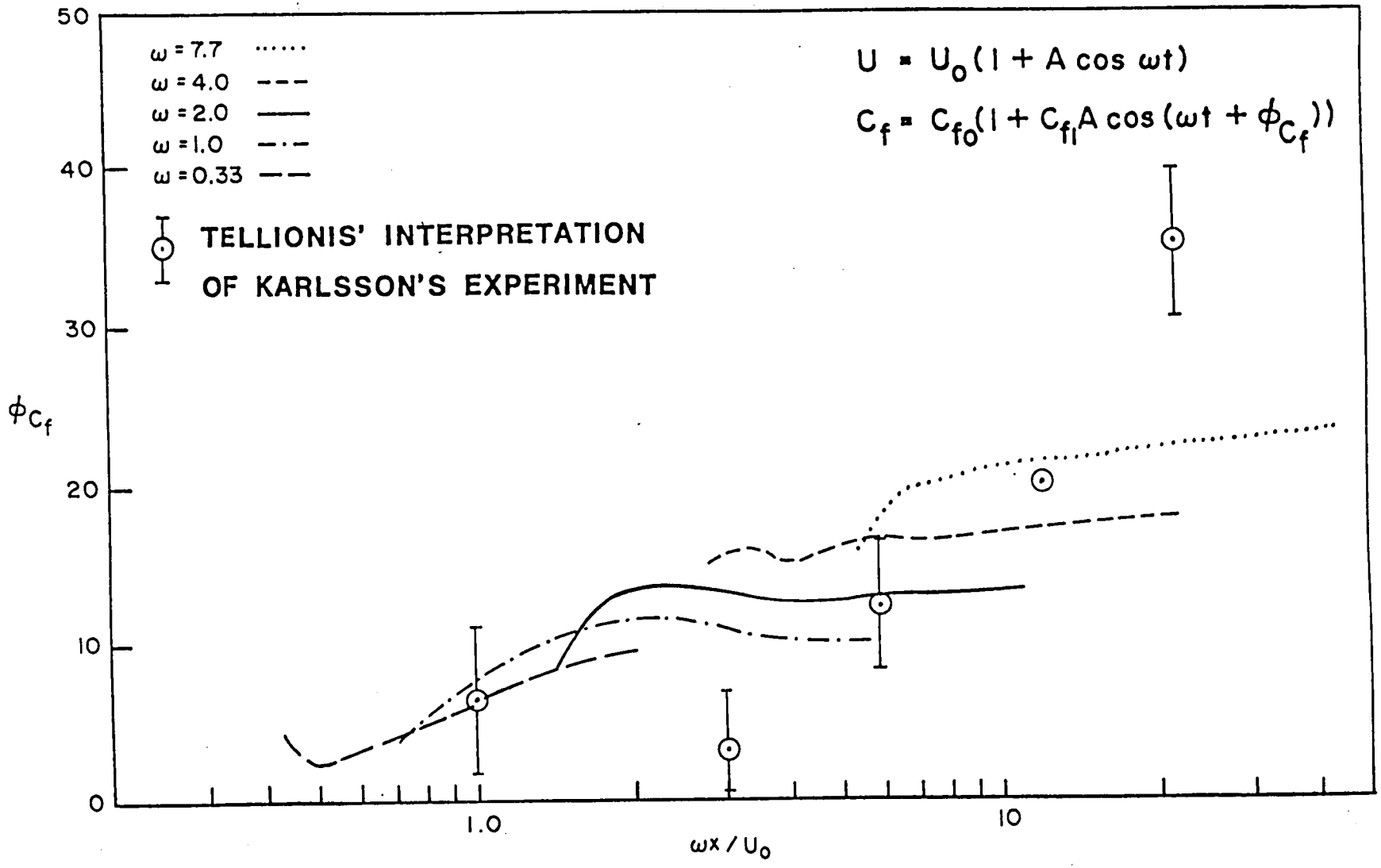

Figure 21 - Phase Angle of Skin Friction Fluctuations

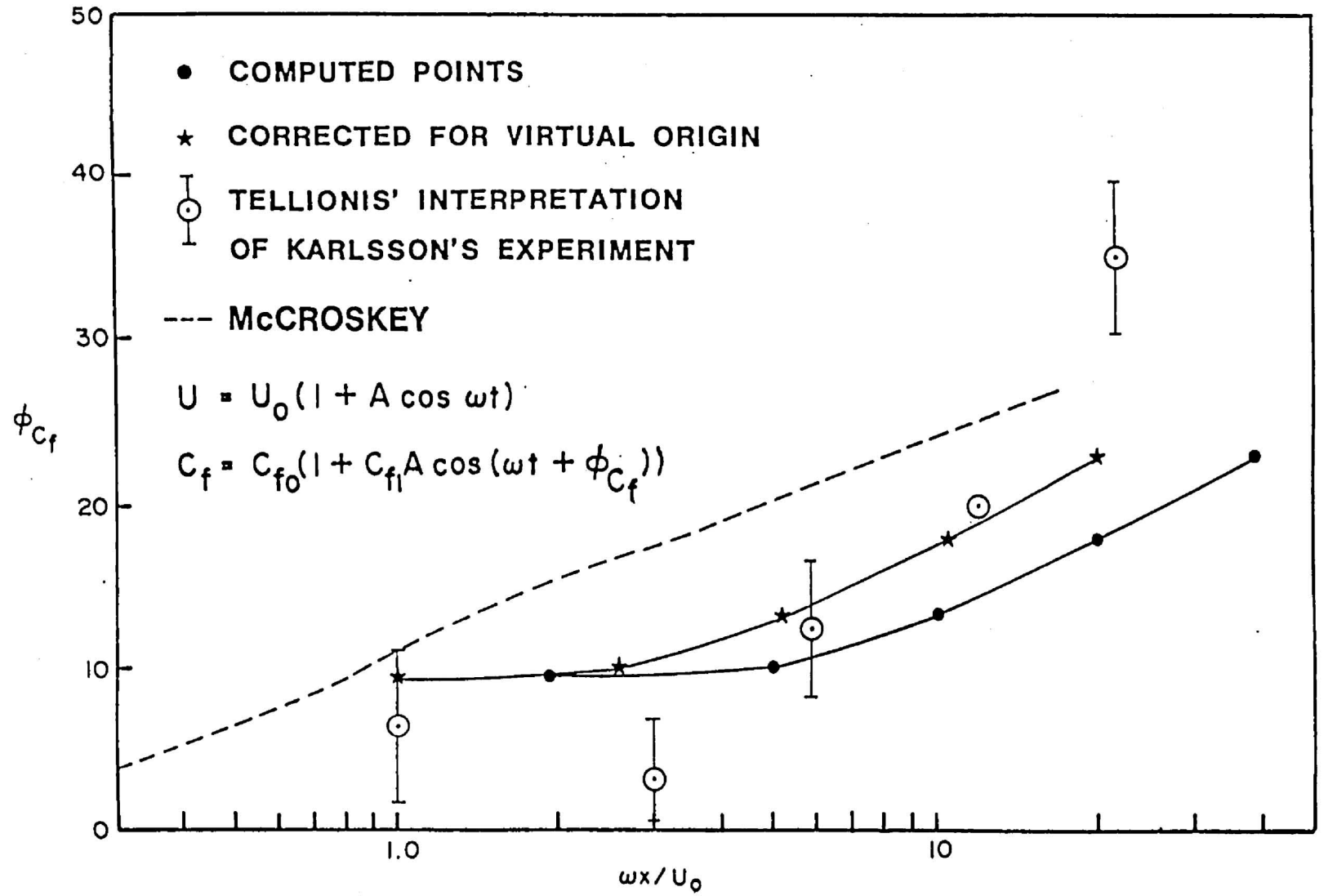

Figure 22 - Phase Angle of Skin Friction Fluctuations - Effect of Virtual Origin

	ϕ_{C_f}	C_{f_1}	ϕ_{δ^*}	δ_1^*
2-D FINE	9.169°	2.134	31.48°	.9170
2-D COARSE	9.127°	2.153	30.86°	.9168
3-D PLANES 9, 14	9.191°	2.134	31.66°	.9145
10, 13	9.195°	2.134	31.62°	.9148
11, 12	9.195°	2.134	31.57°	.9153
12, 11	9.192°	2.134	31.50°	.9157
13, 10	9.186°	2.135	31.45°	.9162
14, 9	9.181°	2.135	31.41°	.9168
MAX. DIFF.	.0028	.0005	.0057	.0027

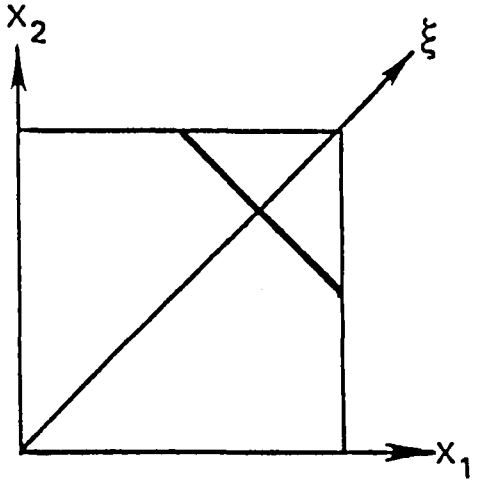

Table 1 - Comparison of Three-Dimensional Results

			RUN TIME	
	GRID	TIME STEPS	TOTAL	PER GRID POINT / TIME STEP
2–D	36 X51 (1836)	108	44.91	.00024
3–D	14 X 14 X 41 (8036)	36	185.35	.00064

Table 2 - Computer Run Times

1. Report No.	2. Government Accession No.	3. Recipient's Catalog No.
NASA CR-172368		

4. Title and Subtitle	5. Report Date
THREE-DIMENSIONAL UNSTEADY VISCOUS FLOW ANALYSIS OVER AIRFOIL SECTIONS	June 1984
	6. Performing Organization Code
7. Author(s)	8. Performing Organization Report No.
B. C. Weinberg and S. J. Shamroth	R84-900027F
	10. Work Unit No.
9. Performing Organization Name and Address	
Scientific Research Associates, Inc. P.O. Box 498 Glastonbury, CT 06033	11. Contract or Grant No. NAS1-17573
	13. Type of Report and Period Covered
12. Sponsoring Agency Name and Address	Contractor report
National Aeronautics and Space Administration Washington, DC 20546	14. Sponsoring Agency Code

15. Supplementary Notes

Langley Technical Representative: John W. Edwards
Final Report

16. Abstract

A three-dimensional solution procedure for the approximate form of the Navier-Stokes equation was exercised in the two- and three-dimensional modes to compute the unsteady turbulent boundary layer on a flat plate corresponding to the data of Karlsson. The procedure is based on the use of a consistently split Linearized Block Implicit technique in conjunction with a QR operator scheme. New time-dependent upstream boundary conditions were developed that yielded realistic solutions for the interior in the vicinity of the upstream boundary. Comparisons of the computation employing these boundary conditions with the data indicate that both qualitative and quantitative agreement was obtained for the mean velocity and the in phase and out of phase components of the first harmonic of the velocity. In addition, the calculation gave results for the skin friction phase angle that had expected physical behavior for large distances downstream of the inflow boundary. For the three-dimensional case, the two-dimensional data of Karlsson was considered, but in a coordinate system skewed at 45° to the free stream direction. The results of the calculations were in excellent agreement with the data and the two-dimensional computations.

17. Key Words (Suggested by Author(s))	18. Distribution Statement
Three-Dimensional Unsteady Turbulent	Unclassified - Unlimited

19. Security Classif. (of this report)	20. Security Classif. (of this page)	21. No. of Pages	22. Price
Unclassified	Unclassified	67	A04

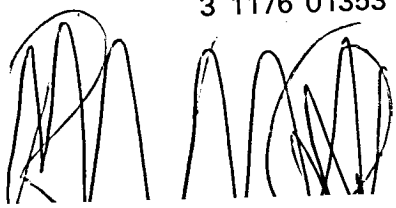

DO NOT REMOVE SLIP FROM MATERIAL

Delete your name from this slip when returning material to the library.

NAME	MS
Satman	173
M.A. Scott 7/97	132

NASA Langley (Rev. May 1988) RIAD N-75